ASCA and ROSAT observations of nearby cluster cooling flows

S.W. Allen[1], A.C. Fabian[1], R.M. Johnstone[1], K.A. Arnaud[2] and P.E.J. Nulsen[3,4]

1. Institute of Astronomy, Madingley Road, Cambridge CB3 0HA
2. Laboratory for High Energy Astrophysics, Goddard Space Flight Center, Greenbelt, MD 20771, USA
3. Department of Engineering Physics, University of Wollongong, Wollongong NSW 2522, Australia
4. Harvard-Smithsonian Center for Astrophysics, 60 Garden Street, Cambridge MA 02138, USA

arXiv:astro-ph/9910188v2   20 Oct 2000

ABSTRACT

We present a detailed analysis of the X-ray properties of the cooling flows in a sample of nearby, X-ray bright clusters of galaxies using high-quality ASCA spectra and ROSAT X-ray images. We demonstrate the need for multiphase models to consistently explain the spectral and imaging X-ray data for the clusters. The mass deposition rates of the cooling flows, independently determined from the ASCA spectra and ROSAT images, exhibit reasonable agreement. We confirm the presence of intrinsic X-ray absorption in the clusters using a variety of spectral models. We also report detections of extended 100μm infrared emission, spatially coincident with the cooling flows, in several of the systems studied. The observed infrared fluxes and flux limits are in good agreement with the predicted values due to reprocessed X-ray emission from the cooling flows. We present precise measurements of the abundances of iron, magnesium, silicon and sulphur in the central regions of the Virgo and Centaurus clusters. Our results firmly favour models in which a high mass fraction $(70 - 80$ per cent$)$ of the iron in the X-ray gas in these regions is due to Type Ia supernovae. Finally, we present a series of methods which may be used to measure the ages of cooling flows from the X-ray data. The results for the present sample of clusters indicate ages of between 2.5 and 7 Gyr. If the ages of cooling flows are primarily set by subcluster merger events, then our results suggest that in the largest clusters, mergers with subclusters with masses of ~ 30 per cent of the final cluster mass are likely to disrupt cooling flows.

Key words: galaxies: clusters: general – cooling flows – intergalactic medium – X-rays: galaxies

1 INTRODUCTION

In the central regions of most clusters of galaxies, the cooling time of the hot intracluster medium is significantly shorter than a Hubble time (Edge, Stewart & Fabian 1992; White, Jones & Forman 1997; Peres *et al.* 1998). This is normally taken to indicate the presence of a cooling flow, in which the hot gas cools and is deposited throughout the cluster core (see Fabian 1994 for a review). Cooling flows are a phenomenon most easily studied at X-ray wavelengths, where the bulk of the cooling occurs. However, large Faraday rotation measures, consistent with cooling-flow models, are also detected in radio observations of cluster cores (Taylor, Barton & Ge 1994; Taylor, Allen & Fabian 1999) and strong optical emission-line nebulosities and UV/blue emission, associated with young, massive stars, are commonly observed in and around the dominant galaxies at the centres of cluster cooling-flows (*e.g.* Johnstone, Fabian & Nulsen 1987; Mc-

Namara & O'Connell 1989; Allen 1995; Cardiel *et al.* 1995, 1998; Crawford *et al.* 1999). The mass in young stars within the central $5 - 20$kpc regions of cooling-flow clusters typically accounts for $\lesssim 10$ per cent of the total mass inferred to be deposited by the cooling flows within their cooling radii $(r_{\rm cool} \sim 50 - 200kpc)$ although can account for a significant fraction of the material deposited within the innermost part. At present, however, the fate of the cooling gas at larger radii remains uncertain (Daines, Fabian & Thomas 1994; Fabian, Johnstone & Daines 1994a; O'Dea *et al.* 1994; Voit & Donahue 1995; O'Dea & Baum 1996; Henkel & Wiklind 1998; Allen 2000; Ferland, Fabian & Johnstone 2000).

The X-ray surface brightness profiles of cooling-flow clusters require that the deposition of cooled matter is typically distributed throughout the cooling radii with $\dot{M} \propto r$. This requires that cooling flows are multiphase (Nulsen 1986; Thomas, Fabian & Nulsen 1987). Spatially-resolved

X-ray spectroscopy, carried out with the Position Sensitive Proportional Counter (PSPC) on ROSAT, has shown that the mean emission-weighted temperatures of cooling-flow clusters decrease towards their centres (*e.g.* Allen & Fabian 1994; Nulsen & Böhringer 1995). More detailed multiphase spectral studies with ASCA have also revealed the presence of at least two gas phases in the central regions of cooling-flow clusters, with a ratio of emission measures in good agreement with the predictions from cooling-flow models (*e.g.* Fukazawa *et al.* 1994; Fabian *et al.* 1994b; Allen 2000).

Early studies based on ASCA spectra for small samples of bright, nearby cooling flows (*e.g.* Fabian *et al.* 1994b) were complicated by uncertainties associated with the calculation of the Fe-L emission-line complex used in plasma emission codes. These calculations have since been significantly improved in the MEKAL code of Kaastra & Mewe (1993; incorporating the Fe L calculations of Liedhal, Osterheld & Goldstein 1995, although residual uncertainties in the calculations of other potentially important elements remain). Further complications in the modelling of the X-ray spectra arise from abundance gradients (*e.g.* Fukazawa *et al.* 1994; Matsumoto *et al.* 1996; Allen & Fabian 1998), the effects of intrinsic absorption (*e.g.* White *et al.* 1991; Allen & Fabian 1997; Wise & Sarazin 2000) and temperature variations within the flows, which depend upon the details of the local gravitational potentials.

In this paper we study ASCA spectra and ROSAT X-ray imaging data for seven bright, nearby cooling flows; the Perseus Cluster (Abell 426), Abell 496, the Virgo Cluster, the Centaurus Cluster (Abell 3526), Abell 1795, 2199 and 2597. We also include one non-cooling flow cluster, the Coma Cluster (Abell 1656), for comparison purposes. Our primary goal is to determine the properties of the cooling flows, using the improved MEKAL code in both our spectral and imaging analyses. We examine regions of the clusters large enough to encompass the entire cooling flows, thereby minimizing systematic problems associated with modelling the complex point spread functions of the ASCA mirrors and the underlying spatial distributions of the X-ray emitting and absorbing gas.

Section 2 of this paper describes the observations and data reduction. Sections 3 and 4 discuss the method and basic results from the spectral analysis. Section 5 examines the enrichment history of the ICM in the central regions of the Virgo and Centaurus clusters. Section 6 describes the deprojection analysis of the imaging data. Section 7 presents a comparison of the properties of the cooling flows determined from the independent spectral and imaging methods. The evidence for intrinsic X-ray absorption and reprocessed emission at infrared wavelengths are explored. Section 8 examines the constraints that may be placed on the ages of cooling flows from the X-ray data. Section 9 discusses the possible role of heating process in cooling flows and the likely effects of subcluster merger events. The most important conclusions from our work are summarized in Section 10. Throughout this paper, we assume $H_0 = 50$ km s^{-1} Mpc^{-1}, $\Omega = 1$ and $\Lambda = 0$. For the Virgo Cluster, a distance of 18Mpc is assumed.

2   OBSERVATIONS AND DATA REDUCTION

2.1   The ASCA observations

The ASCA (Tanaka, Inoue & Holt 1994) observations were made over a three-and-a-half year period between 1993 May and 1996 December. The ASCA X-ray telescope array (XRT) consists of four nested-foil telescopes, each focussed onto one of four detectors; two X-ray CCD cameras, the Solid-state Imaging Spectrometers (SIS; S0 and S1) and two Gas scintillation Imaging Spectrometers (GIS; G2 and G3). The XRT provides a spatial resolution of ~ 3 arcmin (Half Power Diameter) in the energy range $0.3 - 12$ keV. The SIS detectors provide excellent spectral resolution $[\Delta E/E = 0.02(E/5.9\text{keV})^{-0.5}]$ over a 22×22 arcmin^2 field of view. The GIS detectors provide poorer energy resolution $[\Delta E/E = 0.08(E/5.9\text{keV})^{-0.5}]$ but cover a larger circular field of view of ~ 50 arcmin diameter.

For our analysis of the ASCA data we have used the screened event lists from the rev1 processing of the data sets available on the GSFC ASCA archive (for a detailed description of the rev1 processing see the GSFC ASCA Data Reduction Guide, published by GSFC.) The ASCA data were reduced using the FTOOLS software (version 3.6) issued by GSFC, from within the XSELECT environment (version 1.3). Further data-cleaning procedures as recommended in the ASCA Data Reduction Guide, including appropriate grade selection, gain corrections and manual screening based on the individual instrument light curves, were followed. A summary of the ASCA observations, including the individual instrument exposure times after all screening procedures were carried out, is given in Table 1.

Spectra were extracted from all four ASCA detectors (except for Abell 1795 where the S1 data were lost due to saturation problems caused by flickering and 'hot' pixels in the CCDs). The spectra were extracted from circular regions, centred on the peaks of the X-ray emission. For the SIS data, the radii of the regions used were selected to minimize the number of chip boundaries crossed (thereby minimizing the systematic uncertainties introduced by such crossings) whilst covering as large a region of the clusters as possible. Data from the regions between the chips were masked out and excluded. The final extraction radii for the SIS data are summarized in Table 2. The Table also notes the chip modes used for the observations (1,2 or 4 chip mode) and the number of chips from which the extracted data were drawn. For the GIS data, a fixed extraction radius of 6 arcmin was adopted.

Background subtraction was carried out using the 'blank sky' observations of high Galactic latitude fields compiled during the performance verification stage of the ASCA mission. The background data were screened and grade selected in the same manner as the target observations and the background spectra were extracted from the same regions of the detectors as the cluster spectra. (We assume that the errors associated with the background subtraction are statistical in origin.) For the SIS data, response matrices were generated using the FTOOLS SISRMG software. Where the spectra covered more than one chip, response matrices were created for each chip and combined to form a counts-weighted mean matrix. For the GIS analysis, the response matrices issued by GSFC on 1995 March 6 were used. For both the SIS and GIS data, auxiliary response files were

generated with the ASCAARF software, with effective area calculations appropriate for extended sources.

2.2 The ROSAT Observations

The ROSAT observations were carried out between 1991 February and 1994 August. For the more distant systems at redshifts $z \geq 0.03$, the observations were made with the High Resolution Imager (HRI), which provides a ~ 5 arcsec (FWHM) X-ray imaging facility covering a $\sim 40 \times 40$ arcmin^2 field of view (David *et al.* 1996). For the clusters at lower redshifts, the PSPC was used, which has a lower angular resolution (~ 25 arcsec FWHM) but provides a larger (2×2 degree^2) field of view and enhanced sensitivity to extended, low-surface brightness X-ray emission. Using this combination of detectors both good spatial resolution and a field of view extending beyond the cooling radii in all clusters was obtained.

The reduction of the data was carried out using the Starlink ASTERIX package. For the HRI data, X-ray images were extracted on a 2×2 arcsec^2 pixel scale. For the PSPC observations, only data in the $0.4 - 2.0$ keV band were used, and the images were extracted with a pixel scale of 15×15 arcsec^2. Where more than one observation of a source was made, a mosaic was constructed from the individual observations. In each case the data were cleaned and corrected for telescope vignetting and accurate centres were determined for the X-ray emission from the clusters. A summary of the ROSAT observations and the coordinates of the X-ray centroids is supplied in Table 3.

3 SPECTRAL ANALYSIS OF THE ASCA DATA

3.1 The basic spectral models

The modelling of the X-ray spectra has been carried out using the XSPEC spectral fitting package (version 9.0; Arnaud 1996). For the SIS data, only counts in pulse height analyser (PHA) channels corresponding to energies between 0.6 and 10.0 keV were included in the analysis (the energy range over which the calibration of the SIS instruments is best-understood). For the GIS data, only counts in the energy range $1.0 - 10.0$ keV were used. The spectra were grouped before fitting to ensure a minimum of 20 counts per PHA channel, allowing χ^2 statistics to be used.

The spectra have been modelled using the plasma codes of Kaastra & Mewe (1993; incorporating the Fe L calculations of Liedhal, Osterheld & Goldstein 1995) and the photo-electric absorption models of Balucinska-Church & McCammon (1992). The data from all four detectors were included in the analysis, with the fit parameters linked to take the same values across the data sets. The exceptions to this were the emission measures of the ambient cluster gas in the four detectors which, due to the different extraction radii used and residual uncertainties in the flux calibration of the instruments, were maintained as independent fit parameters.

The spectra were first examined with a series of four, basic spectral models: model A consisted of an isothermal plasma in collisional equilibrium at the optically-determined redshift for the cluster, and absorbed by the nominal Galactic column density (Dickey & Lockman 1990). The free parameters in this model were the temperature (kT) and metallicity (Z) of the plasma (measured relative to the solar photospheric values of Anders & Grevesse 1989, with the various elements assumed to be present in their solar ratios) and the emission measures in each of the four detectors. The second model, model B, was the same as model A but with the absorbing column density (N_H) also included as a free parameter in the fits. The third model, model C, included an additional component explicitly accounting for the emission from the cooling flows in the clusters. The material in the cooling flows was assumed to cool at constant pressure from the ambient cluster temperature, following the prescription of Johnstone *et al.* (1992). The normalization of the cooling-flow component was parameterized in terms of a mass deposition rate ($\dot{M}_\mathrm{S}$), which was a free parameter in the fits (linked to take the same value in all four detectors). The metallicity of the cooling gas was assumed to be equal to that of the ambient cluster gas. The emission from the cooling flow was also assumed to be absorbed by an intrinsic column density, ΔN_H, of cold gas, which was a further free parameter in the fits. The abundances of metals in the absorbing material were fixed to their solar values (Anders & Grevesse 1989).

The fourth spectral model, model D, was similar to model C except that the constant-pressure cooling flow component was replaced with a second isothermal emission component. Model D constitutes a more general model which should normally provide an adequate description of the more specific cooling-flow models at the spectral resolution and signal-to-noise ratios typical of ASCA observations (see discussion in Section 3.4). The temperature and normalization of the second, cooler emission component were included as free parameters in the fits (although the normalization of the second emission component was linked to take the same value in all four detectors). The second emission component was again assumed to be intrinsically absorbed by a column density, ΔN_H, of cold gas, which was a further free parameter in the fits. The metallicities of the two emission components were assumed to be equal.

Fig. 1 shows the ASCA data and best-fitting spectral models for four of the clusters in the sample; Abell 426, the Virgo cluster, the Centaurus cluster and Abell 2199. For clarity, only the results for the S1 and G2 detectors are shown. Table 4 summarizes the fit results for the clusters, using the four basic spectral models. We note that the S0 and G3 data for the Centaurus Cluster and the S0 and S1 data for Abell 2597 were found to exhibit small (~ 1 per cent) gain mis-calibrations, for which corrections were applied.

3.2 Isothermal cooling flow models

The constant pressure cooling flow model (model C) provides a crude approximation to the X-ray emission spectrum from a multiphase cooling flow. Recently, Nulsen (1998) has presented a more sophisticated, self-similar model for the emission from a cooling flow in which the mean gas temperature remains constant with radius *i.e.* an 'isothermal' cooling flow. Although the isothermal cooling-flow model is rather specific, the assumption of an approximately constant mass-weighted temperature over the bulk of the radius in a cluster cooling flow is consistent with current constraints on the distribution of gravitating matter in the core regions of

massive clusters from X-ray and gravitational lensing studies (Allen 1998) and with previous, spatially-resolved spectroscopic X-ray studies of nearby clusters cooling flows with ASCA (*e.g.* Fukazawa *et al.* 1994; Ohashi *et al.* 1997; Ikebe *et al.* 1999). The assumption of an approximately isothermal mean gas temperature in cooling flows also leads to a more plausible implied distribution of initial density inhomogeneities in the cluster gas than would be the case if the temperature profiles dropped significantly within the core regions (Thomas, Fabian & Nulsen 1987).

We have incorporated the Nulsen (1998) isothermal cooling flow model into the XSPEC code and applied it to the ASCA data. As with the constant pressure cooling flow model (model C), the isothermal cooling-flow model introduces only two extra free parameters into the fits over and above those present in the single-phase spectral model (model B); the mass deposition rate ($\dot{M}_S$) and the column density of intrinsic X-ray absorbing material (ΔN_H). Note, however, that whereas in the case of the constant pressure cooling flow model the tabulated temperatures are the upper temperatures from which the gas cools, for the isothermal cooling flow models the quoted temperatures are the mean temperatures ($\overline{T}$ from the work of Nulsen 1998) in the cooling flows, which are directly related to the gravitational potentials. (For a comparison of the emission spectra from isothermal and constant pressure cooling flow models see Nulsen 1998).

For our initial analysis, we assumed that the slope of the mass deposition profile, $\eta = 1$ (where $\dot{M} \propto r^\eta$). The mean temperature of the gas in the isothermal cooling flows was linked to be equal to that of the ambient gas at larger radii in the clusters (which, as with spectral models A–D, was a free fit parameter). The results determined with the isothermal cooling flow model with $\eta = 1$ (hereafter spectral model E) are listed in Table 4. In most cases, the isothermal cooling flow model provides at least as good a fit to the ASCA spectra as the constant pressure model (model C), although for the Virgo cluster spectral model C provides a better fit. We note that for the Virgo cluster, the central ~ 5 arcmin radius (S0) aperture analysed corresponds to a spatial scale of only ~ 25 kpc. For this system, it seems plausible that the gravitational potential may flatten significantly in the region studied, and that the approximation of isothermality in the mass-weighted X-ray temperature profile may no longer hold.

We have also investigated the effects on the spectral fits of using other values of η, in the range $0.75 - 2.5$. These results are shown in Table 5. As discussed in Section 8.3, a value of $\eta \sim 1.5$ provides a good match to the image deprojection analysis results for a number of the clusters studied, with statistically acceptable values spanning the range 0.75 to 2.5. The effect of increasing the value of η in the isothermal cooling flow models is always to increase the value of the mass deposition rate and to increase the intrinsic absorption required on that component. The Virgo cluster shows the largest increase in mass deposition rate; a factor of two when increasing η from 0.75 to 2.5. Other clusters show more moderate increases of $20 - 70$ per cent. In general, the value of χ^2 also decreases as η is increased. (The decrease in some cases is statistically significant when increasing η from 0.75 to 2.5.) Abell 426 is the only cluster for which a minimum in χ^2 is found. In most cases the reduction in χ^2 continues

to implausibly high values of η. We do not find a significant improvement in χ^2 when increasing η from the value $\eta = 1.0$ used in model E to the value of $\eta = 1.5$, the most likely value for several of the clusters determined from the imaging data.

In what follows, we will adopt the results determined with spectral model E ($\eta = 1$) as our 'best' spectral results on the cooling flows, except for the Virgo Cluster for which the results determined with the constant pressure model (model C) are preferred.

3.3 The requirement for multiphase models and excess absorption

The results determined from the basic spectral analysis, summarized in Table 4, show that (with the exception of Abell 1795) the fits with the single-temperature models (A and B) are significantly improved (*i.e.* a significant reduction in χ^2 is obtained) when the absorbing column density acting along the line of sight is included as a free parameter in the fits. (For guidance, a reduction of $\Delta\chi^2 \sim 7$, in a fit with $\nu \sim 1000$ degrees of freedom and a reduced chi-squared value $\chi^2_\nu \sim 1.00$, is significant at approximately the 99 per cent confidence level.) A further highly significant reduction in χ^2 is obtained for all clusters when including either an absorbed cooling flow spectrum (models C, E) or an absorbed, cooler isothermal emission component (model D) in the modelling. (For guidance, improvements in χ^2 of ~ 10 and 15, with the introduction of 2 (models C, E) and 3 (model D) extra fit parameters, are significant at approximately the 99 per cent confidence level in a fit with $\nu \sim 1000$ and $\chi^2_\nu \sim 1.00$.)

The requirement for the introduction of cooler emission and absorption components is also illustrated in Fig. 2, where we show the residuals (the data divided by the model predictions, in units of χ) from fits to the individual SIS spectra at energies above 3 keV, using a simple, single temperature model with Galactic absorption (model A). The best-fitting models have then been extrapolated to cover the full $0.6 - 10.0$ keV band of the SIS detectors. In all cases, except the non cooling-flow Coma cluster, a clear excess in the residuals is observed at energies between ~ 0.8 and 3.0 keV. This region of the spectrum is dominated by the Fe-L, Mg, Si and S line complexes, and the detection of positive residuals due to these features provides a clear indication of the presence of gas significantly cooler than the ambient cluster temperature. In addition, the residuals for a number of the clusters exhibit a clear deficit at low energies ($E \lesssim 0.8$ keV) providing evidence for excess absorption, over and above that due to our own Galaxy, associated with the central regions of the clusters.

The temperatures and metallicities determined from the fits to the SIS data in the $3 - 10$ keV energy range are summarized in Table 6. The results are in good agreement with those determined from the more-sophisticated, multiphase analyses of the full ASCA data sets, using spectral models C, D and E.

The residual diagram for Abell 426, determined from the $3 - 10$ keV SIS data using the nominal (Dickey & Lockman 1990) value for the Galactic column density ($N_H = 1.49 \times 10^{21}$ atom cm^{-2}), shows a strong excess of emission below an energy, $E \sim 0.8$ keV (see the dotted points in Fig.

2). We suspect this excess to be due to an over-estimation of the Galactic column density in the region covered by the ASCA spectra, which is significantly smaller than the resolution of the HI studies (Dickey & Lockman 1990). In order for the residual diagram for Abell 426 to appear like those for the other clusters included in this study, a Galactic column density of $\sim 1.0 \times 10^{21}$ atom cm^{-2} is required (solid points in Fig. 2). The ROSAT PSPC X-ray colour ratio study of the Perseus cluster by Allen & Fabian (1997) also suggests a Galactic column density in the region of the cluster core of $\sim 1.1 \times 10^{21}$ cm^{-2}. The $100\mu m$ IRAS map of the Perseus cluster is complex (the system lies at a Galactic latitude of $b = -13$ degrees) and allows for a decrease in the Galactic column density towards the cluster centre. The result on the reduced Galactic column density for Abell 426 is also supported by the detailed modelling of the full ASCA data sets with spectral models C, D and E, which determine values in the range $0.8 - 1.2 \times 10^{21}$ atom cm^{-2}. The results on the Galactic column densities for the other clusters are in reasonable agreement with the values determined from the HI studies (Dickey & Lockman 1990).

3.4 A note on two-temperature models

The results listed in Table 4 show that the two-temperature spectral model (model D) generally provides a slightly better description of the ASCA spectra than the cooling-flow models (C, E). This has sometimes been taken to indicate that the cluster gas is distinctly two-phase, with the cooler phase being due to the central galaxy (*e.g.* Makishima 1997; Ikebe *et al.* 1999). However, the longevity of such a gas phase implied by the common occurrence of cooling flows would then require the presence of a heat source to carefully balance the radiative cooling. The very high cooling rates found in some distant, luminous clusters (*e.g.* Allen 2000) are also difficult to explain with such models.

The fact that the two-temperature models often provide a better description of the ASCA data is not, a priori, surprising. Model D provides a more general fitting parameterization for multi-temperature plasmas observed with ASCA, with an extra degree of freedom over the cooling flow models. Simulated cooling-flow spectra, constructed at the spectral resolution and with count statistics comparable to those of typical ASCA observations, are well-described by two-temperature models (*e.g.* Allen 2000; see also Buote, Canizares & Fabian 1999). Where spectral model D provides a significantly better fit to the observations than models C and E, this need only indicate that the simple cooling flow models over-simplify the true emission spectra from the central regions of the clusters. In particular, given that the systems studied here are the nearest, X-ray brightest cluster cooling flows, in which strong radial variations in metallicity and intrinsic absorption are known exist (Fukazawa *et al.* 1994, Matsumoto *et al.* 1996, Allen & Fabian 1997) and in which clear deviations from solar abundance ratios are observed (Section 5), the fact that the basic cooling-flow models over-simplify the observed situation is to be expected.

We note that for the very best ASCA data sets, such as the observation of the Centaurus Cluster presented here, the data are of sufficient quality to demonstrate the presence of more than two thermal components. Section 4 discusses the evidence for additional power-law components in the fits

with the two-temperature plasma models. For the Centaurus Cluster, the fit with the two-temperature plus power-law model (also incorporating variable element abundance ratios; see Section 5) is further improved by the introduction of a third plasma component. Following Allen, Di Matteo & Fabian (2000) and using only the data from the S1 and G2 detectors for the fits incorporating the power-law components (which are the best calibrated detectors for that particular observation, the S0 and G3 data sets exhibiting noticeable gain offsets; Section 3.1), we find that the introduction of the third plasma component (which is assumed to be absorbed by the same intrinsic column density as the power-law and the cooler of the two initial plasma components) leads to a drop in χ^2 of $\Delta\chi^2 = 37$ for the introduction of 2 additional degrees of freedom. The best fit temperatures in this case are 3.25, 1.51 and 0.64 keV, respectively.

3.5 Comparison with previous results

A number of previous works have also presented results based on ASCA observations of the central regions of the clusters studied here. Fabian *et al.* (1994b) report results from an early analysis of ASCA data for the innermost regions of the Perseus (Abell 426), Centaurus and Coma clusters and Abell 1795. The regions studied by Fabian *et al.* (1994b) were smaller than those studied here and did not include the the entire cooling flows. For this reason the mass deposition rates measured by Fabian *et al.* (1994b) are approximately a factor two smaller than those reported here.

Fukazawa *et al.* (1994) present an analysis of a previous, shorter ASCA observation of central regions of the Centaurus Cluster (the same data studied by Fabian *et al.* 1994b). These authors reported the discovery of a strong metallicity gradient in the cluster, with a central metallicity and temperature in good agreement with the results presented here. Ikebe *et al.* (1999) present results from a detailed analysis of the longer, more recent observation of the Centaurus Cluster also studied in this paper. Their results from fits with two-temperature models incorporating variable element abundance ratios are in good general agreement with those reported here (Section 5).

Matsumoto *et al.* (1996) present an analysis of ASCA observations of the central regions of the Virgo Cluster. Their results for the innermost regions of the cluster, determined using a two temperature model with variable element abundances, are in reasonable agreement with those reported here, although small systematic differences exist. These differences are presumably due to the different plasma codes used in the two studies. The MEKAL code (Kaastra & Mewe 1993; Liedhal, Osterheld & Goldstein 1995) employed in this paper contains significant improvements over the Raymond & Smith (1977) code used in the earlier Matsumoto *et al.* (1996) work. Our results on the temperature and abundance structure in the central regions of the Virgo and Centaurus clusters are in good agreement with the recent results of Buote *et al.* (1999).

Xu *et al.* (1998) report results from a study of the central regions of Abell 1795 with ASCA. Their results, obtained using a simple, two-temperature model are in good agreement with those reported here from our analysis with spectral model D. The temperature in the central regions of the Coma cluster determined with spectral model B is

in good agreement with the previous result of Honda *et al.* (1996).

Markevitch *et al.* (1998, 1999) present detailed results on the temperature structure in Abell 496, 1795, 2199 and 2597. These authors determine mean temperatures, corrected for the effects of cooling flows, for these clusters of 4.7 ± 0.2, 7.8 ± 1.0, 4.8 ± 0.2 and $4.4^{+0.4}_{-0.7}$ keV, respectively. In general, the mean cluster temperatures measured by Markevitch *et al.* (1998, 1999) are slightly hotter than the results for the central regions of the clusters reported here, using spectral models C and E (the cooling-flow models).

4   THE EVIDENCE FOR POWER-LAW COMPONENTS

Allen *et al.* (2000) and Di Matteo *et al.* (2000) have previously reported the detection of hard, power-law emission components in the ASCA data for the Virgo and Centaurus clusters. The presence of these components is clearly evident in the residual diagrams shown in Fig. 2. We have extended this analysis to the other higher luminosity systems reported here. Starting in each case with the best-fitting two temperature model, we have examined the improvements to the fits obtained by introducing an additional power-law emission component.[⋆] The photon index and normalization of the power-law components were included as free fit parameters. (Note that for the Virgo and Centaurus clusters, the best fitting two-temperature models incorporating variable element abundances were used as the starting points for the analysis; see Section 5). The power-law components were assumed to be absorbed by the same intrinsic column density as the cooler thermal emission components.[†] The results from the fits are summarized in Table 7.

The results for Abell 426 and 2597 suggest the presence of relatively luminous power-law components ($L_{X,1-10} = 4.0^{+0.3}_{-0.4} \times 10^{44}$ and $2.0^{+1.1}_{-0.9} \times 10^{44}$ erg s^{-1}, respectively)

[⋆] We use the two-temperature model (model D) as the starting point for our analysis of the power-law components since it provides the most flexible fitting parameterization for the cluster emission, and therefore the most rigorous test for the presence of additional power-law components. The two-temperature model also allows for the inclusion of variable element abundance ratios (using the *vmekal* model in XSPEC), which is firmly required by the data for the Virgo and Centaurus clusters (Section 5). We note that the inclusion of a power-law component into the fits with the cooling flow emission models (models C and E) also leads to significant improvements in χ^2 and constraints on the power-law components consistent with those listed in Table 7 (although for Abell 496 the inferred $2-10$ keV flux is approximately twice as high and the χ^2 value +46 worse). For the Virgo and Centaurus clusters, Abell 1795 and 2199, the mass deposition rates determined with the cooling flow-plus-power-law models are in good agreement with the values listed in Table 4, although for Abell 426, 496 and 2597, the rates are reduced by a factor ≥ 1.6.

[†] The ASCA spectra cannot easily constrain more complex spectral models in which the intrinsic column density acting on the power-law component is included as a separate free parameter, although such models are probably more realistic. The intrinsic column densities associated with the power-law components measured with such models are, however, likely to be larger than the values listed in Table 7).

with photon indices ($\Gamma = 2.05^{+0.05}_{-0.05}$ and $1.80^{+0.42}_{-0.66}$) consistent with the typical values determined for Seyfert nuclei (*e.g.* Nandra *et al.* 1997). However, the flux associated with the power-law component in Abell 426 ($F_{X,2-10} = 1.80^{+0.12}_{-0.14} \times 10^{-10}$ erg cm^{-2} s^{-1}) is approximately an order of magnitude larger than the nuclear point-source flux inferred from ROSAT HRI observations of the dominant cluster galaxy, NGC 1275, made in 1991 February and 1994 August (using the same spectral model). This implies either the presence of significant intrinsic absorption associated with the nucleus of NGC 1275 (see also Section 7.3), that the power-law emission originates (at least in part) from some other source, or some other deficiency with the spectral model.

The results for Abell 496, 1795 and 2199 are more analogous to those those previously reported for the Virgo and Centaurus clusters. For Abell 496, we measure a photon index, $\Gamma = 1.44^{+0.44}_{-0.38}$ and an intrinsic $1-10$ keV luminosity associated with the power-law component of $3.29^{+1.49}_{-0.84} \times 10^{43}$ erg s^{-1}, which is ~ 80 times larger than the value for M87. The results for Abell 1795 and 2199 indicate marginal improvements to the fits with the introduction of hard, power-law components, with intrinsic $1-10$ keV luminosities of ~ 6 and 3.5×10^{43} erg s^{-1}, respectively. In all three cases the ASCA data allow for significant intrinsic absorption acting on power-law emission, which is consistent with the fact that a central point sources appear to contribute only weakly in the ROSAT band.

Comparing the results in Table 7 with those in Table 4, we see that the most noticeable effect on the best-fit parameter values measured with spectral model D, on the introduction of the power-law component, is to decrease the temperature of the hotter thermal component to a value in better agreement with the results obtained using the cooling flow models, C and E. For Abell 426, the mean metallicity is also increased from $\sim 0.5Z_\odot$ to $0.8Z_\odot$, which is consistent with the presence of a metallicity gradient in the cluster, albeit with the caveats given above. (We note that the relatively poor χ^2 value for Abell 426 is primarily caused by residuals in the S0 data. If we repeat our analysis of Abell 426 incorporating the power-law component but excluding the S0 data, we obtain similar best-fit parameters and $\chi^2 = 1570$ for 1398 degrees of freedom.)

4.1   Power-law emission from the Coma Cluster

The spectral fit to the Coma Cluster with spectral model D was not improved by the introduction of an additional power-law component. We are able to place a 90 per cent confidence upper limit on the flux of any power-law component (with a canonical AGN photon index $\Gamma = 2.0$) incorporated into model D of $F_{X,2-10} < 2.2 \times 10^{-12}$ erg cm^{-2} s^{-1}. However, the introduction of a power-law component was found to significantly improve the fit obtained with the more simple, single-temperature spectral model B ($\Delta\chi^2 = 9.0$, giving $\chi^2 = 1265$ for 1225 degrees of freedom). The best-fit photon index and normalization for the power-law component, determined using the single-temperature plus power-law model, are $\Gamma = 3.3^{+0.9}_{-1.6}$ and $A_1 = 3.1^{+4.0}_{-1.7} \times 10^{-3}$ photon keV^{-1}cm^{-2}s^{-1}. The mean cluster temperature measured with this model is $8.5^{+0.6}_{-0.5}$ keV. The 90 per cent confidence upper limits on the flux associated with the power-law com-

ponent in the $2-10$ and $20-80$ keV bands are 1.9×10^{-11} and 3.1×10^{-11} erg cm^{-2} s^{-1}, respectively.

Fusco-Femiano *et al.* (1999) report the detection of hard, non-thermal X-ray emission from the the Coma Cluster using observations made with the Phoswhich Detection System (PDS) and High-Pressure Gas Scintillation Proportional Counter (HPGSPC) on the BeppoSAX satellite. (The PDS and HPGSPC detectors have fields of view ~ 1.3 (hexagonal) and 1.0 degree across, respectively.) From a joint fit to the PDS and HPGSPC data, which together cover the $4.5-80$ keV range, using a single-temperature plus power-law model, these authors determine a mean temperature for the ICM of $8.5^{+0.6}_{-0.5}$ keV, and a best-fitting power-law photon index of $\Gamma = 1.7 - 3$. The $20 - 80$ keV flux associated with the power-law component (measured from the PDS data alone) is $\sim 2.2 \times 10^{-11}$ erg cm^{-2} s^{-1}. These parameters are consistent with those determined from the ASCA data, using the same simple spectral model.

Rephaeli, Gruber & Blanco (1999) also report observations of the central ~ 1 degree region of the Coma Cluster using the Proportional Counter Array (PCA) and High-Energy X-ray Timing Experiment (HEXTE) on the Rossi X-ray Timing Explorer (RXTE). Rephaeli *et al.* (1999) show that the RXTE data in the $3-100$ keV range can be equally well-modelled using either a two-temperature plasma model (with temperatures of $8.2^{+2.0}_{-1.2}$ and $4.7^{+1.6}_{-3.0}$ keV, respectively; with the cooler component accounting for ~ 20 per cent of the total flux) or a single-temperature plus power-law model. In this second case (favoured by the authors), the RXTE data measure a mean cluster temperature of 7.51 ± 0.18 keV and a photon index and normalization (at 1 keV) associated with the power-law component of $\Gamma = 2.35 \pm 0.45$ and $A_1 = 1.9 \pm 0.4 \times 10^{-2}$ photon keV^{-1}cm^{-2}s^{-1}, respectively. This normalization is somewhat higher than that measured from the ASCA data, which may indicate that the source of the power-law emission in this cluster is more extended than the regions included in the ASCA analysis.

5 THE ABUNDANCES OF ELEMENTS IN THE VIRGO AND CENTAURUS CLUSTERS

5.1 The observed abundances ratios

The metallicities and abundance ratios of the various elements in the ICM place firm constraints on the enrichment history of the cluster gas and the relative contributions from different types of supernovae. Mushotzky *et al.* (1996) reported results from an ASCA study of the outer regions of four nearby clusters (Abell 1060, AWM7 and the same observations of Abell 496 and 2199 presented here) and concluded, based on the mean metallicities of O, Ne, Si, S and Fe determined from their work, that most of the enrichment in the outer regions of clusters is likely to be due to Type II supernovae. However, these authors warned that a significant contribution from Type Ia supernovae could not be ruled out. Subsequent analyses of clusters and groups (Finoguenov & Ponman 1999; Dupke & White 2000a,b) have shown that their central regions often exhibit enhanced contributions from Type Ia supernovae.

The high-quality ASCA spectra for the Centaurus and Virgo clusters analysed here provide an excellent opportu-

nity to re-examine the issue of individual element abundances in the ICM in nearby clusters. (The SIS data for the Centaurus and Virgo clusters provide the most significant and reliable constraints of the eight systems examined here and we therefore concentrate our discussion on these two clusters). Using the S0 and S1 data for the Virgo cluster, and the S1 data for the Centaurus Cluster (the data sets which are best-calibrated and most sensitive for the present task), and starting in each case with the best fitting two-temperature model (Model D; which has the abundances of all other elements linked to be equal to that of iron), we have systematically determined the improvements to the fits obtained by allowing the metallicity of each element, in turn, to be included as a free parameter in the fit. Having identified the element giving the most significant improvement, the metallicity of that element was maintained as a free parameter, and the process repeated to determine the element providing the next most significant improvement. This was continued until no further significant improvement (at > 95 per cent confidence, as determined using an F-test) was obtained by allowing other elements to fit freely.

For the Virgo cluster, the most significant improvement to the fit to the joint S0 and S1 data with spectral model D was obtained by including the abundance of Mg as a free fit parameter (χ^2 drops from 757.7 to 570.4). This was followed by Si (giving a further drop in χ^2 to 511.5), Na ($\chi^2 = 488.8$) and S ($\chi^2 = 468.9$). At this point including the abundances of further elements as free parameters did not significantly improve the fit.

For the Centaurus cluster, the most significant improvement in the fit to the S1 data was also initially obtained by allowing the abundance of Mg to fit freely (χ^2 drops from 478.4 to 409.5). This was followed, in turn, by O ($\chi^2 = 369.3$), Si ($\chi^2 = 339.0$) and S ($\chi^2 = 322.3$).

The results on the abundances of the individual elements in the central regions of the Centaurus and Virgo clusters are summarized in Table 8. The two-dimensional confidence contours on the abundances of Mg, Si, S and Fe in the Virgo Cluster are shown in Fig. 3. The fits with the free-fitting element abundances provide highly significant improvements in the goodness-of-fit with respect to the values determined with the basic two-temperature model (model D). However, the best-fitting temperatures (kT and kT_2), Galactic column densities (N_H) and intrinsic column densities (ΔN_H) are in good, general agreement with those listed in Table 4. The measured Galactic column densities are also in good agreement with the values determined from HI studies (Dickey & Lockman 1990). We note that the results on the element abundances are not significantly modified by the inclusion of the power-law components discussed in Section 4.

Our results on the [Si/Fe] and [S/Fe] ratios in the central regions of the Virgo cluster are in good agreement with the previous measurements of Matsumoto *et al.* (1996; although the absolute element abundances differ, presumably due to the different plasma models used in the two studies; Section 3.5). Our results on the Si, S and Fe abundances in the central regions of the Centaurus cluster are similar to those reported by Ikebe *et al.* (1999). The measured Si, S and Fe abundances in both the Virgo and Centaurus clusters are in good agreement with the results of Buote *et al.* (1999).

We caution against over-interpretation of the result on the low oxygen abundance for the Centaurus Cluster. This result is primarily due to features at the lowest energies in the S1 spectrum, where systematic errors and complexities due to absorption in the cluster are at a maximum. Similarly, the result on the high Na abundance in the Virgo cluster (11 ± 3 times the solar value) is due to a line-like emission feature at $E \sim 1.25$keV in the spectrum, where residual uncertainties in the modelling of the Fe-L emission complex remain.

The element abundances most reliably determined from our data are those of Fe, Mg, Si and S. For the Virgo cluster we determine abundance ratios (using the solar photospheric abundance scale of Anders & Grevesse 1989) of [Mg/Fe]=-0.45 (with values in the range -0.67 to -0.28 being consistent with the joint 90 per cent confidence limits on the individual abundance measurements), [Si/Fe]=0.18 (0.12-0.24) and [S/Fe]=0.10 (0.03-0.17). For the Centaurus cluster we determine [Mg/Fe]=-0.49 (with a 90 per cent confidence range of -0.82 to -0.25), [Si/Fe]=0.14 (0.07-0.22) and [S/Fe]=0.13 (0.05-0.22). Thus, we find the abundance ratios for the Virgo and Centaurus clusters to be both well constrained and in excellent agreement with each other.

Our results on the abundance ratios for [Mg/Fe], [Si/Fe] and [S/Fe] in the inner regions of the Centaurus and Virgo clusters differ from those of Mushotzky *et al.* (1996) from their study of the outer regions of other nearby clusters observed with ASCA. Mushotzky *et al.* (1996) determined mean abundance ratios for [Mg/Fe]=0.07, [Si/Fe]=0.31 and [S/Fe]=-0.11 from their sample, using the same solar photospheric abundance scale. The differences between these results are consistent with the changes in the relative abundances with radius inferred to be present in other clusters (*e.g.* Dupke & White 2000b).

5.2   Comparison with supernovae enrichment models

Recently, a number of studies (Ishimaru & Arimoto 1997; Gibson, Lowenstein & Mushotzky 1997; Nagataki & Sato 1998; Dupke & White 2000a) have presented detailed predictions for the $\alpha-$element abundances in the ICM, as a function of the fraction of the iron enrichment due to type Ia supernovae, using a variety of theoretical supernovae models. Scaling the observed abundance ratios for the central regions of the Centaurus and Virgo clusters to the meteoric abundance scale of Anders & Grevesse (1989), as used in the theoretical calculations, we determine mean, un-weighted abundance ratios of [Mg/Fe] ~ -0.63, [Si/Fe] ~ 0.00 and [S/Fe]~ 0.02. Thus, the [Si/Fe] and [S/Fe] ratios in the central regions of the Centaurus and Virgo clusters are in good agreement with the solar meteoric values. In contrast, the observed [Mg/Fe] ratio indicates that magnesium is ~ 4 times under-abundant with respect to the meteoric value.

Comparing these results with the predictions of Nagataki & Sato (1998), our observed [Si/Fe] ratio implies a mass fraction of the iron enrichment due to type Ia supernovae, $M_{\rm Fe,SNIa}/M_{\rm Fe,total}$, in the range $M_{\rm Fe,SNIa}/M_{\rm Fe,total} \sim 0.6 - 0.9$ (where the limits cover the full range of supernovae models studied by those authors). A similar comparison of the observed [Si/Fe] result with the range of models discussed by Gibson *et al.* (1997) also requires

$M_{\rm Fe,SNIa}/M_{\rm Fe,total} \sim 0.6 - 0.8$. The observed, mean [Mg/Fe] ratio favours a mass fraction due to type Ia supernovae of $M_{\rm Fe,SNIa}/M_{\rm Fe,total} \gtrsim 0.7$ (Gibson *et al.* 1997).

A comparison of the observed [S/Fe] ratio ([S/Fe]~ 0.02) with the theoretical models of Nagataki & Sato (1998) requires $M_{\rm Fe,SNIa}/M_{\rm Fe,total} = 0.4 - 0.8$, for spherical type II supernovae explosions. However, the lower sulphur yields associated with aspherical type II explosion models imply somewhat lower $M_{\rm Fe,SNIa}/M_{\rm Fe,total}$ values, depending on the degree of asphericity and the precise SNIa enrichment model used. In particular, the observed [S/Fe] ratio appears inconsistent with enrichment models incorporating both a high degree of asphericity in the SNeII explosions and simple deflagration of the type Ia supernovae (Nagataki & Sato 1998). Comparing the observed [S/Fe] value with Gibson *et al.* (1997) indicates $M_{\rm Fe,SNIa}/M_{\rm Fe,total} \lesssim 0.7$. In contrast to previous results (Mushotzky *et al.* 1996; Gibson *et al.* 1997), our observations do not indicate a severe deficiency of sulphur with respect to the other α-elements, when compared with the theoretical predictions (at least for models incorporating relatively low degree of asphericity in the type-II supernovae).

In summary, the observed $\alpha-$element abundance ratios in the central regions of the Centaurus and Virgo clusters favour a high mass fraction of the observed iron abundance being due to type Ia supernovae, with a value $M_{\rm Fe,SNIa}/M_{\rm Fe,total} \sim 0.7 - 0.8$ providing consistent results.

5.3   Type Ia supernovae and the formation of metallicity gradients

Spatially resolved spectroscopy of the Centaurus and Virgo clusters has revealed the presence of strong metallicity gradients in the central regions of these systems (Fukazawa *et al.* 1994, Matsumoto *et al.* 1996). Similar gradients have also been reported in a number of other nearby cooling flows *e.g.* Abell 496 (Hatsukade *et al.* 1997) and AWM7 (Ezawa *et al.* 1997). Allen & Fabian (1998) showed that the mean emission weighted metallicity of luminous cooling-flow clusters is approximately twice that of non cooling-flow systems, which is most plausibly understood as being due to the presence of metallicity gradients in the cooling flow systems. In contrast, ASCA observations of nearby, non-cooling flow clusters and clusters with relatively small cooling flows *e.g.* the Coma Cluster (Watanabe *et al.* 1997), Abell 1060 (Tamura *et al.* 1996) and the Ophiuchus Cluster (Matsuzawa *et al.* 1996), show little or no metallicity gradients.

The results on the individual element abundances in the central regions the Centaurus and Virgo Clusters shows that, where the metallicity gradients exist, the enrichment of the ICM is primarily due to type-Ia supernovae. The mechanism by which metallicity gradients form in cooling-flow clusters remains unclear, but may be due to one or more of galaxy stripping, continuous enrichment by supernovae within the central galaxy, or a Type Ia supernova wind from the central galaxy (Dupke & White 2000b). The absence of metallicity gradients in non-cooling flow systems appears related to recent or ongoing subcluster merger events in these systems, which will disrupt and mix the central high metallicity gas with the surrounding lower-metallicity material (Allen & Fabian 1998). The presence of a metallicity gra-

dient then appears a standard property of regular, relaxed clusters which also, invariably, contain cooling flows.

The presence of a cooling flow may act either to enhance or reduce any metallicity gradient present in a cluster, with the details depending on how well the metals are mixed with the cooling gas. If the mixing is good then as the metals are injected or deposited into the cluster environment they will primarily enrich the least dense X-ray gas at any radius, since this gas will have the largest volume filling factor. This less-dense material will flow furthest in towards the cluster center in the cooling flow, whereas the denser, less-enriched material will be deposited at larger radii. Reisenegger, Miralda-Escudé & Waxman (1996) discuss such a model for the production of the metallicity gradient observed in the Centaurus Cluster, wherein the observed enrichment is primarily due to type Ia supernovae within the central cluster galaxy. A prediction of their model is that metallicity gradients should be most obvious in relatively low X-ray luminosity clusters, with higher ratios for their stellar/X-ray gas mass contents, which appears consistent with the detections of strong gradients in the Centaurus and Virgo clusters, Abell 496 and AWM7. If the mixing of metals with the ICM is poor, however, localized regions of high metallicity material may cool faster than the surrounding gas, leading to the gradual reduction of any metallicity gradient apparent in the X-ray data, and to a decrease in the mean, emission-weighted metallicity of the cluster. Further discrimination on the origin of metallicity gradients in cooling flow clusters will be possible using observations made with the Chandra Observatory and XMM-Newton.

6 DEPROJECTION ANALYSIS OF THE ROSAT IMAGES

The analysis of the ROSAT images has been carried out using an extensively updated version of the deprojection code of Fabian *et al.* (1981; see also White *et al.* 1997). Azimuthally-averaged X-ray surface brightness profiles were determined for each cluster from the ROSAT images. These profiles were background-subtracted, corrected for telescope vignetting and re-binned to provide sufficient counts in each annulus for the deprojection analysis to be extended beyond the cooling radii.

With the X-ray surface brightness profiles as the primary input, and under assumptions of spherical symmetry and hydrostatic equilibrium, the deprojection technique can be used to study the basic properties of the intracluster gas (temperature, density, pressure, cooling rate) as a function of radius. The deprojection code uses a monte-carlo method to determine the statistical uncertainties on the results and incorporates the appropriate HRI and PSPC spectral response matrices issued by GSFC. The cluster metallicities were fixed at the values determined from the spectral analysis and the absorbing column densities were initially set to their respective Galactic values.

The deprojection code requires the total mass profiles for the clusters, which define the pressure profiles, to be specified. We have iteratively determined the mass profiles that result in deprojected temperature profiles (which approximate the mass-weighted temperature profiles in the clusters) that are isothermal within the regions probed by the

ROSAT data and which are consistent with the best-fit temperatures determined from the ASCA spectra with spectral model E (or spectral models C and D for the Virgo and Coma clusters, respectively; Section 3). The validity of the assumption of isothermal mass-weighted temperature profiles in the cluster cores is discussed by Allen (1998). The use of approximately isothermal deprojected temperature profiles also allows for a direct comparison between the mass deposition rates from the cooling flows determined from image deprojection and spectral analyses (see Section 7.1).

The dominant components of the cluster mass profiles have been parameterized using the model for an isothermal sphere given in Equation 4-125 of Binney & Tremaine 1987) with adjustable core radii, $r_{\rm c}$, and velocity dispersions, σ. The core radii were adjusted until the deviations from isothermality in the deprojected temperature profiles were minimized. The velocity dispersions were then adjusted until the temperatures determined from the deprojection code came into agreement with the values measured from the spectral analyses. An initial estimate for the pressure in the outermost radial bin used in the analysis is also required by the deprojection code, although the uncertainties in these values do not significantly affect the results.

For several of the clusters, these simple single-component mass models could not adequately satisfy the requirement for isothermal deprojected temperature profiles, particularly in the central regions of the clusters. However, for these systems it was also found that the introduction of a second 'linear' mass component (providing a constant contribution to the total mass per kpc radius *cf* Thomas *et al.* 1987) significantly improved the fits. These linear components (which may be intuitively associated with the central dominant galaxies in the clusters) were truncated at outer radii of 20 kpc. Their normalizations were adjusted iteratively (together with the $r_{\rm c}$ and σ values) in order to obtain the best match to the required isothermal temperature profiles.

The mass distributions determined from the deprojection analysis are summarized in columns $3-5$ of Table 9. The errors on the velocity dispersions are the range of values that result in isothermal deprojected temperature profiles that are consistent, at the 90 per cent confidence limit, with the spectrally-determined temperatures. These results may be used to provide direct comparisons with independent mass constraints from dynamical studies. We note that the mean core radius for the mass distributions in the cooling flow clusters of 48 ± 15 kpc is in good agreement with the value of ~ 50 kpc determined from the combined X-ray and gravitational lensing study of more distant, luminous lensing clusters by Allen (1998).

7 THE PROPERTIES OF THE COOLING FLOWS

In the following Section, we examine the basic properties of the cooling flows in the clusters. We compare the mass deposition rates determined from the spectral and image deprojection methods. We examine the evidence for intrinsic X-ray absorption in the clusters and compare our results with those from previous studies. Finally, we report detections of extended infrared emission, spatially coincident with

the cooling flows, in several of the systems studied. The observed infrared fluxes and flux limits are shown to be in good agreement with the predicted values due to reprocessed X-ray emission from the cooling flows.

7.1   The mass deposition rates

The spectral and image deprojection analyses presented in Sections 3 and 6 provide essentially independent estimates of the mass deposition rates in the clusters. A comparison of the results obtained from these analyses therefore provides a firm test of the validity of the cooling flow model.

The deprojection method describes the X-ray emission from a cluster as arising from a series of concentric spherical shells. The luminosity in a particular shell, j, may be written as the sum of four components (Arnaud 1988).

$$L_j = \Delta \dot{M}_j H_j + \Delta \dot{M}_j \Delta \Phi_j + \left[\sum_{i=1}^{j-1} \Delta \dot{M}_i (\Delta \Phi_j + \Delta H_j) \right], \quad (1)$$

where $\Delta \dot{M}_j$ is the mass deposited in shell j, H_j is the enthalpy of the gas in shell j, and $\Delta \Phi_j$ is the gravitational energy released in crossing that shell. $\sum_{i=1}^{j-1} \Delta \dot{M}_i$ is the mass flow rate through shell j, and ΔH_j the change of enthalpy of the gas as it moves through that shell. The first term in equation 1 thus accounts for the enthalpy of the gas deposited in shell j. The second term is the gravitational work done on the gas deposited in shell j. The third and fourth terms respectively account for the gravitational work done on material flowing through shell j to interior radii, and the enthalpy released by that material as it passes through the shell.

In any particular shell, the densest material in the cooling flow is assumed to cool out and be deposited. Since the cooling time of this material will be short compared to the flow time, the cooling can be assumed to take place at a fixed radius. Thus, the luminosity contributed by the first term in equation 1 should have a spectrum appropriate for gas cooling at constant pressure from the ambient cluster temperature *i.e.* the same spectrum as the cooling flow component in spectral model C (Section 3). For the bulk of the material continuing to flow inwards towards the cluster centre, the cooling via X-ray emission is assumed to be offset by the gravitational work done on the gas as it moves inwards. The emission accounted for in the second and third terms of equation 1 should therefore have a spectrum that can be approximated by an isothermal plasma at the appropriate ambient temperature for the cluster *i.e.* the spectrum of the isothermal emission component also included in model C. Since the mass-weighted temperature profiles in the clusters are assumed to remain approximately isothermal with radius, the luminosity contributed by the fourth term of equation 1 should be relatively small. Overall, the integrated emission from the cooling flow can be expected to have a spectrum similar to that described by spectral model E. (In general, the results on the mass deposition rates determined with spectral models C and E show good agreement; Table 4.)

The mass deposition rates determined from the deprojection analysis ($\dot{M}_{\rm I}$; Table 9) are the mass inflow rates measured at the cooling radii in the clusters *i.e.* the radii at which the cooling time of the cluster gas first exceeds a Hubble time (1.3×10^{10} yr). Thus, if the cooling flow model is correct, and if the cooling flows have existed for a significant fraction of a Hubble time, the mass deposition rates determined from the deprojection analysis should be comparable to the values measured independently from the spectral data.

Fig. 4(a) shows the mass deposition rates determined from the spectral analysis ($\dot{M}_{\rm S}$) versus the results from the deprojection study ($\dot{M}_{\rm I}$). In all cases, except the Virgo Cluster, we have used the spectral results determined with model E as the ordinate, since this is the more physical of the two cooling flow models and typically provides at least as good a fit to the data as the constant pressure approximation.

The results plotted in Fig. 4(a) exhibit an approximately linear correlation. A fit to the data with a power-law model of the form $\dot{M}_{\rm S} = P \dot{M}_{\rm I}^Q$, using the Akritas & Bershady (1996) bisector modification of the ordinary least-squares statistic (which accounts for the possibility of intrinsic scatter in the data) gives a best-fitting slope, $Q = 1.15 \pm 0.33$ and a normalization, $P = 0.36 \pm 0.65$ (where the errors are the standard deviations determined by bootstrap re-sampling).

The spectral analysis presented in Section 3 also indicates that the cooling gas is intrinsically absorbed by equivalent hydrogen column densities of, typically, a few 10^{21} atom cm^{-2}. In principle, therefore, the mass deposition rates determined from the deprojection analysis should also be corrected for the effects of this absorbing material. Such corrections, however, depend upon both the spatial distribution and nature of the absorbing material, which at present remain uncertain. Nevertheless, under the specific assumption that the intrinsic absorption is due to cold gas which lies in a uniform screen in front of the cooling flows, the effects of intrinsic absorption on the deprojection results may be estimated.

The corrections for intrinsic absorption due to a uniform foreground screen of cold gas have been carried out by re-running the deprojection code with the absorbing column densities set to the total values determined with spectral model E (model C for the Virgo Cluster). Since the intrinsic column densities measured with model E are redshifted quantities, we have set the total column densities used in the revised deprojection analysis, which assumes zero redshift for the absorber, to values $N_{\rm H} + \Delta N_{\rm H}/(1+z)^3$, where $N_{\rm H}$ is the Galactic column density.) The absorption-corrected mass deposition rates ($\dot{M}_{\rm C}$) so determined are summarized in Table 10. Fig. 4(b) compares the results on the mass deposition rates from the spectral analysis with the absorption-corrected deprojection values. A fit to the data with a power-law model of the form $\dot{M}_{\rm S} = P \dot{M}_{\rm C}^Q$ gives a slope, $Q = 1.09 \pm 0.32$ and a normalization, $P = 0.18 \pm 0.37$ (where the errors are the standard deviations determined by bootstrap re-sampling).

We conclude that the results on the mass deposition rates determined from the spectral and imaging methods exhibit an approximately linear correlation and marginal agreement in normalization in the case where no corrections for intrinsic absorption on the imaging results are made. The application of simple correction factors, appropriate for absorption by a uniform screen of cold gas, lead to the imaging results exceeding the spectral values by typical factors

of $\sim 2 - 4$, although the details of these corrections remain highly uncertain at present. As we shall discuss in Section 8, an improved agreement between the imaging and spectral results on the mass deposition rates is obtained once the different ages of the cooling flows are also accounted for in the analysis.

7.2 Intrinsic X-ray absorption

The negative residuals at low energies ($E < 0.8$keV) in Fig. 2 provide a clear indication of the presence of excess absorption, over and above the nominal Galactic values (Dickey & Lockman 1990) along the lines of sight to the clusters. The analyses of the full ASCA data sets with spectral models B, C, D and E also indicate the presence of intrinsic X-ray absorbing material in the clusters. However, the precise column density measurements, summarized in Table 11, are sensitive to the spectral model used.

Using the simple isothermal model with free-fitting absorption (model B), we measure a mean excess column density for the seven cooling-flow clusters of $2.4 \pm 2.8 \times 10^{20}$ atom cm^{-2}. We note that the value measured for the Perseus Cluster (Abell 426) is negative, supporting the conclusion drawn in Section 3.3 that the nominal Galactic column density determined from HI studies ($N_\mathrm{H} = 1.49 \times 10^{21}$ atom cm^{-2}; Dickey & Lockman 1990) overestimates the true column density along the line of sight to the cluster core. Interestingly, the excess column density measured for the Coma cluster ($1.5 \pm 0.5 \times 10^{20}$ atom cm^{-2}) is consistent with the mean value determined for the cooling-flow clusters, using the same spectral model. Our results on the excess column densities measured with spectral model B may be compared to the 90 per cent confidence upper limits on the size of any systematic excess column density present in the S0 and S1 detectors due to calibration errors of $< 8 \times 10^{19}$ and $< 2 \times 10^{20}$ atom cm^{-2}, respectively (Orr *et al.* 1988; these values are valid for observations made before mid 1996. See also Dotani *et al.* 1996).

The results on the intrinsic column densities for the cooling-flow clusters are quite different, however, when the more-sophisticated multiphase spectral models (C, D and E) are used. As discussed in Section 3, models C, D and E generally provide a significantly better fit to the ASCA data for the cooling-flow clusters than the simple single-phase models (A and B). Using spectral models C and E, which are our preferred models in that they provide a consistent description for the spectral and imaging X-ray data for the clusters (Sections 7.1, 8.3), we measure a mean intrinsic column density acting on the cooling-flow components of $3 - 4 \times 10^{21}$ atom cm^{-2}. Using the two-temperature model (model D) we determine a similar mean intrinsic column density. Thus, the typical intrinsic column densities measured with the multiphase spectral models are approximately an order of magnitude larger than those determined using the single-phase model B. These results are in good agreement with those presented by Allen (2000) from an analysis of larger sample of more luminous, distant cooling flow clusters.

We have also measured the intrinsic column densities in the clusters using one further spectral model, which we refer to as model C'. Model C' is identical to model C except that it assumes that the intrinsic absorption acts on the entire cluster spectrum, rather than just the cooling gas,

and that the absorbing material lies at zero redshift. Model C' has been used in a number of previous studies (*e.g.* White *et al.* 1991; Allen & Fabian 1997) and is included here for comparison purposes. The results obtained for the present sample of clusters using model C' are also listed in Table 11. The mean excess column density for the cooling-flow clusters determined with this model is $4.9 \pm 4.5 \times 10^{20}$ atom cm^{-2}.

Allen & Fabian (1997) presented results from an X-ray colour deprojection study of 18 clusters observed with the ROSAT PSPC, from which they determined intrinsic column densities across the central 30 arcsec (radius) regions of Abell 426, 496, 1795, 2199 and 2597 (using spectral model C') of 0.50 ± 0.55, 2.57 ± 0.62, 2.20 ± 0.20, 2.67 ± 0.25 and $2.36 \pm 0.58 \times 10^{20}$ atom cm^{-2}, respectively. The results for Abell 496, 1795 and 2199 are in reasonable agreement with those presented here, although our value for Abell 2597 is ~ 3 times larger than the Allen & Fabian (1997) result. We note, however, that the ASCA observations of Abell 2597 were carried out in 1996 December and are likely to have been affected by radiation damage to the SIS detectors, which is known to lead to overestimates of the measured column densities in observations made after (approximately) late 1995 (Hwang *et al.* 1999). The Allen & Fabian (1997) result for Abell 426 was determined using a lower value for the Galactic column density of 1.37×10^{21} atom cm^{-2} (Stark *et al.* 1992). If we also adopt this lower value, our ASCA measurement for the intrinsic column density in this cluster, using model C', rises to $0.10^{+0.50}_{-0.40} \times 10^{20}$, consistent with the previous PSPC result.

Six of the cooling-flow clusters included in the present work were also studied by White *et al.* (1991), using Einstein Observatory SSS data. The analysis of the SSS observations (which covered central, three arcmin radius circular apertures in the clusters) was also carried out using spectral model C'. White *et al.* (1991) presented measurements of the intrinsic column densities in Abell 426, 496, 1795, 2199 and the Virgo cluster of 13 ± 2, 20^{+4}_{-2}, 8 ± 3, 14 ± 2 and $15 \pm 2 \times 10^{20}$ atom cm^{-2}, respectively. (The SSS observation of the Centaurus cluster was offset from the centroid listed in Table 3 by ~ 4 arcmin, prohibiting any direct comparison with the present work.) The intrinsic column densities measured by White *et al.* (1991) are significantly larger (by factors ranging from two to $\gtrsim$ an order of magnitude) than the values determined from the ASCA and ROSAT data. The ASCA result for the non-cooling flow Coma cluster, measured with spectral model B, of $\Delta N_\mathrm{H} = 1.5 \pm 0.5 \times 10^{20}$ atom cm^{-2} is consistent with the White *et al.* (1991) limit of $\Delta N_\mathrm{H} < 5 \times 10^{20}$ atom cm^{-2}.

Finally, we have examined the constraints that may be placed on the covering fraction, f, of the intrinsic X-ray absorbing material using the ASCA data. Using spectral model E, we measure a typical best-fit covering fraction of unity and can rule out covering fractions significantly less than 90 per cent. The exception to this is the result for the Virgo cluster, for which we measure a best-fit covering fraction with spectral model E, $f = 0.66^{+0.15}_{-0.16}$ (for spectral model C we find $f = 0.86^{+0.07}_{-0.07}$). The results on the covering fractions, and the agreement of the ASCA and PSPC results, suggest that the White *et al.* (1991) results are likely to have systematically over-estimated the intrinsic column densities in clusters, although the qualitative result on the detection of

significant intrinsic X-ray absorption in cooling-flow clusters is confirmed.

7.3 The luminosity reprocessed in other wavebands

The luminosities absorbed at X-ray wavelengths must eventually be reprocessed in other wavebands. If the absorbing material is dusty (as is likely to be the case in the central regions of the clusters *e.g.* Voit & Donahue 1995; Fabian *et al.* 1994a) then the bulk of this reprocessed emission is likely to emerge in the far infrared. Table 12 summarizes the reprocessed luminosities (*i.e.* the bolometric luminosities absorbed within the clusters) measured with spectral model E (or model C for the Virgo Cluster). The reprocessed luminosities range from $\sim 4 \times 10^{42}$ erg s^{-1} for the Virgo Cluster to $\sim 5 \times 10^{44}$ erg s^{-1} for Abell 2597.

Table 12 also lists the observed 60 and 100μm fluxes within a four arcmin (radius) aperture centred on the X-ray centroids for the clusters (Table 3). The observed fluxes were measured using the IPAC SCANPI software and co-added IRAS scans. (The median of the co-added scans was used.) The root-mean-square deviations in the residuals external to the source extraction regions after baseline subtraction, and the in-scan separations (in arcmin) between the peaks of the 100μm emission and the X-ray centres, are also included in the table.

Three of the clusters listed in Table 12, Abell 426, the Centaurus Cluster and Abell 2199, provide convincing detections of 100μm flux associated with the peaks of their X-ray emission. For the Centaurus cluster and Abell 2199 (and the slightly offset source associated with Abell 496), the infrared emission appears spatially extended. For Abell 426, the detected infrared flux is point-like and presumably associated with the active nucleus of the central galaxy, NGC1275. Cox, Bregman & Schombert (1995) have previously reported detections of infrared emission from the central regions of the Centaurus Cluster and Abell 2199, from an analysis of the same IRAS scan data. These authors did not detect significant (≥ 98 per cent confidence) infrared emission from within 1 arcmin (radius) of the dominant galaxies in Abell 496, 1795 or 2597, which is consistent with our results. The presence of a strong, point-like infrared source in Abell 426 was previously reported by Wise *et al.* (1993) who measured 60 and 100μm fluxes associated with this source of 6.48 and 8.73 Jy, respectively.

Following Helou *et al.* (1988) and Wise *et al.* (1993), the total infrared luminosities in the $1 - 1000\mu$m band may be estimated from the observed IRAS fluxes using the relation

$$L_{1-1000\mu m} \sim 2.8 \times 10^{44} (\frac{z}{0.05})^2 (2.58 S_{60} + S_{100}) \, \text{erg s}^{-1} \,, \quad (2)$$

where S_{60} and S_{100} are the 60 and 100μm IRAS fluxes in units of Jy. This relation assumes a dust temperature of ~ 30K and an emissivity index n in the range $0 - 2$, where the emissivity is proportional to the frequency, ν^n. We associate a systematic uncertainty of ± 30 per cent with the estimated $1 - 1000\mu$m luminosities, which is combined in quadrature with the random errors. (In most cases, the systematic error exceeds the random errors. Note that the systematic errors associated with the measured IRAS fluxes may be $\gg 30$ per cent in some cases *e.g.* see the note on

the Virgo Cluster below.) The $1 - 1000\mu$m luminosities calculated from this relation are summarized in Table 12. Fig. 5 shows the results plotted as a function of the predicted reprocessed luminosities.

For the Centaurus Cluster and Abell 2199, the estimated $1 - 1000\mu$m luminosities are in good agreement with the reprocessed luminosities predicted from the X-ray models. The observed S_{60}/S_{100} flux ratios for these clusters indicate dust temperatures in the range $20 - 50$K. For Abell 426, the $1 - 1000\mu$m luminosity exceeds the predicted reprocessed X-ray luminosity by a factor ~ 4, consistent with the presence of a strong, intrinsically absorbed active nucleus in this system (*cf* Section 4). For Abell 496, the observed flux also exceeds the predicted flux by a factor of ~ 4, although the ~ 3 arcmin spatial offset between the 100μm and X-ray centroids suggests that the infrared emission is likely to originate, at least in part, from some source other than the cooling flow. (This is also evidenced by the implausibly low S_{60}/S_{100} flux ratio measured for the cluster). For the Virgo Cluster, the predicted reprocessed X-ray luminosity exceeds the $1 - 1000\mu$m luminosity determined from the IRAS data by a factor of three. However, this is unsurprising since the SCANPI software is not well suited to measuring fluxes from highly extended objects (the cooling flow in the Virgo Cluster has the largest angular extent of any of the systems studied in this paper, although this may also affect the IRAS results for the Perseus Cluster.) Finally, we note that it if the bulk of the absorbing material in the clusters is very cold ($T < 10$K), as suggested by some models (*e.g.* Johnstone, Fabian & Taylor 1998 and references therein), then a significant fraction of reprocessed emission may emerge in the sub-mm band.

8 MEASURING THE AGES OF COOLING FLOWS

The natural state for a regular, relaxed cluster of galaxies appears to include the presence of a cooling flow in its core (*e.g.* Edge *et al.* 1992; Peres *et al.* 1998). Simulations suggest that cooling flows are only likely to be disrupted to the extent that they are 'turned off' when a cluster merges with a subcluster of comparable size (*e.g.* McGlynn & Fabian 1984). In this section, we discuss three methods which may be used to measure the ages of cooling flows from the X-ray data and apply them to the ASCA and ROSAT observations of the nearby cluster cooling flows.

8.1 Method 1: X-ray colour deprojection

The first constraints on the ages of cooling flows in clusters were presented by Allen & Fabian (1997) from their X-ray colour deprojection study of 18 nearby systems observed with the ROSAT PSPC. These authors used their X-ray colour deprojection technique to measure the spatial distributions of cool(ing) gas in the clusters and compared their results with the predictions from simple, time-dependent cooling flow models. Essentially, Allen & Fabian (1997) identified the ages of the cooling flows with the cooling time of the ICM at the outermost radii at which significant cooling is observed. These authors provide cooling-flow age measurements for seven clusters, four of which are also

included in the present work. Their results for Abell 496, 1795, 2199 and 2597 are $3.3 - 6.8$, $3.6 - 6.7$, $5.3 - 7.7$ and $2.5 - 5.1$ Gyr, respectively.

8.2 Method 2: Comparison of the spectral and imaging mass deposition rates

A second estimate of the ages of cooling flows may be obtained by comparing the essentially independent results on the mass deposition rates determined from the spectral and image deprojection studies. The deprojection analysis, discussed in Section 6, measures the mass deposition profiles in the clusters *i.e.* the mass deposition rates as a function of radius. The integrated mass deposition rates inferred from the deprojection analysis are the mass deposition rates integrated out to some critical radius ($r_{\rm cool}$) at which the mean cooling time of the X-ray gas ($t_{\rm cool}$) becomes equal to an assumed age for the system. (The results presented in Table 9 are for an assumed age of 1.3×10^{10} yr). The spectral data, in contrast, provide a measure of the current, total mass deposition rates in the clusters. Thus, the ages of the cooling flows may simply be associated with the cooling time of the X-ray gas at the radii where the integrated mass deposition rates determined from the deprojection analysis become equal to the values measured directly from the spectral data.

The primary uncertainty with this method lies in the corrections for the effects on intrinsic absorption, especially on the deprojection results. The larger the correction for intrinsic absorption at a particular radius, the larger the mass deposition rate inferred at that radius and, therefore, the smaller the age of the cooling flow. The cooling-flow ages determined with this method, both with and without corrections for intrinsic absorption due to a uniform foreground screen of cold gas on the deprojection analysis, are summarized in columns 3 and 4 of Table 13.

8.3 Method 3: Breaks in the deprojected mass deposition profiles

The X-ray colour deprojection method (method 1) identifies the age of a cooling flow with the mean cooling time of the cluster gas at the outermost radius where the spectral signature of cooling gas is observed. Since the presence of cooling gas will tend to enhance the X-ray luminosity of a cluster, the outermost radius at which cooling occurs may also be expected to be associated with a 'break' in the X-ray surface brightness profile and, more evidently, the mass deposition profile determined from the deprojection analysis.

We have searched for the presence of breaks in the mass deposition profiles determined from the deprojection analysis by fitting these profiles with broken power-law models. Only those data from radii interior to the 90 percentile upper limits to the cooling radii were included in the modelling, with the exception of the Virgo cluster where, due to systematic uncertainties associated with the effects of the detector support structure, the analysis was limited to the central 78 kpc (15 arcmin) radius. An unweighted, ordinary least-squares statistic was used in the fits. (A reduced χ^2 value of 1.0 was assumed in estimating the $\Delta\chi^2 = 2.71$ errors.) The results from the fits are summarized in Table 14.

Several of the clusters studied (*e.g.* Abell 426, 496) exhibit clear breaks in their mass deposition profiles at radii

$r < r_{\rm cool}$. In other systems, the identification of a break radius is less clear, although still formally significant (*e.g.* Abell 2199). Following method 1, we identify the ages of the cooling flows with the mean cooling time of the cluster gas at the break radii. In calculating the ages, we assume that the X-ray emission at the break radii is unaffected by intrinsic absorption, which is reasonable if the absorbing material in the clusters is gradually accumulated by the cooling flows.

The only cluster for which we do not detect a significant break in the mass deposition profile is the Centaurus Cluster which, interestingly, also has the largest age measured with method 2. (The age measurement for the Centaurus Cluster with method 2 is consistent with the cooling flow having survived intact since the cluster was formed. In this case no break in the mass deposition profile is expected). Fig. 6 shows the mass deposition profiles for a representative subsample of the clusters studied, with the best-fitting broken power-law models overlaid. The mean cooling time of the cluster gas as a function of radius is shown in the lower panels.

We have measured the slopes of the mass deposition profiles interior and external to the break radii in the clusters. (These slopes may be used to constrain the range of plausible isothermal cooling flow models discussed in Section 3.2). The mean slope interior to the break radii (*i.e.* in the regions where mass deposition is expected to occur) is 1.37 ± 0.27. Beyond this point, the mean slope flattens to a value of 0.59 ± 0.21.

Finally, in Table 14, we also list the integrated mass deposition rates interior to the break radii, both corrected and uncorrected for absorption due to a uniform foreground screen of cold gas (as described in Section 7.1). Fig. 7 shows these values plotted as a function of the mass deposition rates determined from the spectral data. (The Centaurus Cluster does not exhibit a clear break within the cooling radius and we assume $\dot{M}_{\rm Brk} = \dot{M}_{\rm C}$ or $\dot{M}_{\rm Brk} = \dot{M}_{\rm I}$ from Table 10, as appropriate.) In general, the agreement between the results is good, particularly for the uncorrected data. (Recall that significant uncertainties remain in the corrections for intrinsic absorption, due both to the unknown geometry and physical nature of the absorbing matter. See also Section 9.1). A fit to the results with a power-law model of the form $\dot{M}_{\rm S} = P\dot{M}_{\rm Brk}^Q$, using the Akritas & Bershady (1996) bisector modification of the ordinary least-squares statistic, gives a slope $Q = 1.08 \pm 0.14$ and a normalization, $P = 0.33 \pm 0.25$ for the absorption-corrected data, and a slope $Q = 1.11 \pm 0.19$ and a normalization, $P = 0.70 \pm 0.61$ for the uncorrected results (where the errors are the standard deviations determined by bootstrap re-sampling).

8.4 Comparison of results

Table 13 summarizes the ages for the cooling flows determined using the three different methods. These results are also shown in graphical form in Fig. 8, where we have averaged the absorption-corrected and uncorrected results determined with method 2. In general, the results on the ages show good agreement, suggesting that the individual methods may indeed be used to reliably measure the ages of the cooling flows.

One source of uncertainty with the age measurements is the relation between the cooling time (*i.e.* the time taken for

the gas to cool to zero degrees at constant pressure) of the ICM at the outermost radii where cooling gas is observed and the ages of the cooling flows. In detail, the outermost radius at which significant mass deposition occurs will depend upon the spectrum of density inhomogeneities in the cluster gas, which at present remains unknown.

As discussed above, the effects of intrinsic absorption provide an additional source of uncertainty. In particular, the ages determined with method 2 (the comparison of the spectral and deprojected mass deposition rates) are sensitive to such effects, although the results based on the break radii (method 3) are insensitive to any uniform change in column density across the cooling flows, and those from the X-ray colour deprojection analysis (method 1) are largely independent of column density uncertainties (other than in the determination of the cooling time at the outermost edge of the cooling flows, where we assume zero intrinsic absorption). Future observations with the Chandra Observatory and XMM-Newton will directly address such uncertainties, permitting spatially-resolved spectroscopic determinations of both the mass deposition and intrinsic absorption profiles in clusters on spatial scales $\gtrsim$ a few arcsec.

Taking into account the uncertainties associated with the different methods, we identify method 1 as the most robust, followed by method 3, with method 2 being the most sensitive to systematic effects. Method 1 requires the best data, with good spatial and moderate spectral resolution and a high signal-to-noise ratio. (To date this method has has only been applicable to PSPC observations of a few of the nearest, brightest clusters of galaxies). In contrast, method 3 should be applicable to a large number of ROSAT HRI observations. We note that method 2 is, at present, also complicated by the fact that it combines results from different detectors, which introduces additional systematic uncertainties.

Averaging the absorption-corrected and uncorrected results determined with method 2 (which provides a reasonable estimate of our uncertainty in these quantities) and taking an unweighted mean of the results determined with the three separate methods, we arrive at the following ages for the cooling flows in the clusters: Abell 426 (2.5 Gyr), Abell 496 (5.4 Gyr), the Virgo Cluster (2.6 Gyr), the Centaurus Cluster (7.1 Gyr), Abell 1795 (5.4 Gyr), Abell 2199 (5.9 Gyr) and Abell 2597 (3.2 Gyr).

9   DISCUSSION

9.1   The possible role of heating processes

The age-corrected mass deposition rates determined from the image deprojection analysis, with no corrections for the effects of intrinsic absorption applied, are generally in good agreement with the spectrally-determined values. However, the absorption-corrected, age-corrected deprojection results are typically about a factor of two larger than the spectral measurements. Although this discrepancy may simply be due to incorrect assumptions about the spatial distribution and physical nature of the absorbing medium (Voit & Donahue 1995, Arnaud & Mushotzky 1998 and Allen 2000 discuss the possibility that the intrinsic absorption in clusters may be primarily due to dust grains) it is sensible to also consider other possibilities.

The location of the break radii in the clusters is crucial in measuring the integrated mass deposition rates from the imaging data. One possibility for reducing the imaging values is to associate the ages of the cooling flows with the cooling time of the cluster gas at radii of about one half of the observed break radii. This would, however, lead to significantly shorter ages for the cooling flows, which would be puzzling for a phenomenon which appears to be so common. Moreover the X-ray colour deprojection technique (Method 1) clearly shows that cool(ing) gas extends out to about the break radii. The assumption of constant metallicity within the cooling flows (where significant metallicity gradients are observed; Section 5.3) will also introduce systematic errors, although these are unlikely to result in discrepancies as large as a factor of two. The use of a larger value for η in the isothermal cooling flow spectral models (Table 5) can also slightly reduce the discrepancy between the spectral and absorption-corrected imaging mass deposition rates, but not fully account for it. It remains possible that a combination of some or all of these factors, together with issues such as the correctness of the plasma code, details depending on the assumed element abundances (the current cooling flow models do not account for variable element abundance ratios) and/or the geometry and effects of the magnetic field, are responsible.

A further plausible alternative is that there may be some heating as well as cooling in the central region. Many authors have proposed various heating models (see Fabian 1994 for references) but none has been found to be compelling and essential in the face of the clear spectral evidence for cool, and probably cooling, gas components. Nevertheless the presence of radio sources at the centres of most cooling flows demonstrates that at least some heating occurs. An important point with any viable heating process, given the X-ray observations, is that it must allow some of the gas to continue cooling, which means that the heating rate must be say one third to one half of the total cooling rate. Such a close balance suggests feedback *i.e.* the heat source is fed by the cooling gas.

One obvious solution is that the central engines in the radio sources are fuelled by the flows (Bailey 1980; Nulsen, Stewart & Fabian 1984; Fabian & Crawford 1990). This has the useful properties that the radio sources are spatially extended and can therefore supply heat (probably via low energy cosmic rays, depending on the magnetic topology and connection to the various gas phases, or by shocks) over an extended region, and that the cooling gas fueling the source will, in a multiphase flow, be the hottest phase in which the effects of cosmic ray and/or shock heating are greatest (in general, the hottest phase will have the longest cooling time and shock or cosmic ray heating will increase its cooling time by the greatest absolute amount. Presumably heating will also be strongest near the centre). This hottest phase is then likely to be the phase through which the feedback operates. If there is temporarily too much heating, this may stop the cooling and reduce the central fuel supply to the radio source. Conversely, if there is too little heating the accretion rate onto the nucleus will rise (for a discussion in the context of single-phase gas models see *e.g.* Tucker & David 1997).

Pedlar *et al.* al (1992) and Owen & Eilek (1998) have emphasised the importance of heating by the central radio

sources in the Perseus Cluster and Abell 2199, respectively. Our results provide an indication of the possible strength of this heating in such systems. The heating may occur intermittently, but overall it appears that it may cause up to a factor of two reduction in the total mass deposition rates deduced from the image deprojection method, once absorption corrections have been made. We note that these rates remain close to the values obtained when no absorption correction is made and are therefore similar to the pre-1990 published values, which have always been regarded as uncertain by about a factor of two (*e.g.* Arnaud 1988; Fabian 1994) due to uncertainties in the gravitational potentials of the clusters.

The tentative identification of a heating signature discussed here does not affect the question of what becomes of the cooled material deposited by cooling flows. The spectral evidence from ASCA and other X-ray data suggest that tens to hundreds of solar masses of gas cool out of cooling flows per year. Over the billion year age of a flow this amounts to 5×10^{10} to greater than $10^{12} \, \mathrm{M_\odot}$ of cooled material, of which only a small fraction is directly observed at other wavelengths.

9.2 The masses of merging subclusters that disrupt cooling flows

Observations and theoretical models suggest that cooling flows are likely to be disrupted when a cluster merges with a subcluster of comparable size (*e.g.* McGlynn & Fabian 1984; Edge, Stewart & Fabian 1992; Allen 1998). When the density in the core of the merging subcluster is sufficiently high, the gas in the central regions of the dominant cluster is likely to be shocked and disrupted as the systems merge, leading to complex X-ray morphologies, temperature inhomogeneities and an inflation of the X-ray core radii (Navarro, Frenk & White 1995; Schindler 1996; Roettiger, Burns & Loken 1996). The time taken for the cooling flow to reform after the dark matter distributions merge and hydrostatic equilibrium is restored will depend upon the degree to which cool gas originally present in the central regions of the clusters is heated and mixed with the surrounding ICM. However, the fact that ~ 70 per cent of bright, nearby clusters contain cooling flows (Peres *et al.* 1998) suggests that cooling flows are 'turned off' on average for ~ 30 per cent of the time. In this case, we may expect the typical time taken for a cooling flow to reestablish itself following a major subcluster merger event to be of the order of a few Gyr. Given the results on the ages of the cooling flows presented in Section 8, we may therefore expect the present sample of clusters to have experienced their last major subcluster merger events during the last $5 - 10$ Gyr (with the Coma, Perseus and Virgo clusters having experienced the most recent merger events and the cooling flow in the Centaurus Cluster having been undisturbed for the longest period).

Assuming that subcluster mergers are the primary cause of the disruption of cooling flows, we can estimate the masses of the merging subclusters which cause significant disruption by integrating the merger rates predicted by hierarchical formation models, using parameters appropriate for rich clusters. Such rates are given by the extended Press-Schechter formalism of Lacey & Cole (1993). Exam-

ples of their application to rich clusters are given by Cavaliere, Menci & Tozzi (1999).

The results for a cluster mass of $10^{15} \, \mathrm{M_\odot}$ are shown in Fig. 9, where we plot the fraction of clusters that have undergone a merger with a subcluster of mass greater than $10 - 80$ per cent of the final cluster mass, within a given interval. (We assume $\Omega = 1.0, \Lambda = 0, b = 1$ and a cosmic fluctuation index $n = -1.5$.) It is clear from the figure that for there to have been a good chance ($\gtrsim 50$ per cent) of a merger within the last 10 Gyr, subclusters with masses of $\lesssim 30 - 40$ per cent of the total final mass are required. Major mergers involving subclusters of similar mass (*i.e.* half of the final mass) have a probability of ~ 20 per cent within that time. The results are similar for an open cosmology with $\Omega = 0.3$ (other cosmological parameters the same) for which subclusters with masses of $\lesssim 20 - 30$ per cent of the total, final mass have an $\gtrsim 50$ per cent chance of merging within the last 10 Gyr and the probability of a merger with a subcluster of similar mass is ~ 10 per cent. Thus, if subcluster mergers are the primary cause of the disruption of cooling flows in rich clusters, it seems likely that subclusters with masses of ~ 30 per cent of the final cluster mass can disrupt cooling flows.

The results for a cluster of mass $10^{14} \, \mathrm{M_\odot}$ (a mass similar to that of the lowest luminosity clusters in our sample) show a much higher rate of significant mergers, with a ~ 50 per cent chance of a major merger within the last 5 Gyr. It is therefore not clear why the ages of the cooling flows in the present sample of objects appear roughly independent of their luminosity (and therefore mass). A possible explanation is that mergers may not be the only cause of cooling flow disruption. Activity in the nuclei of the central, dominant galaxies may also be important. If the ages of the cooling flows (taking into account the time required for the flows to settle down) are around 8 Gyr, then the disruption is likely to have occurred at redshift of $z = 1 - 2$ and so could be related to the peak of quasar/radio activity.

The application of similar techniques to future observations made with the Chandra Observatory and XMM-Newton should permit precise measurements of the ages of cooling flows for large samples of clusters within redshifts $z \lesssim 1$.

10 CONCLUSIONS

The main conclusions that may be drawn from this paper may be summarized as follows:

(i) We have demonstrated the need for multiphase models to consistently explain the spectral and imaging X-ray data for the nearest, brightest cooling-flow clusters. In general, the diffuse, thermal emission from these systems can be modelled using either two temperature or cooling flow models, with excess absorption acting on the cooler emission components.

(ii) The mass deposition rates for the cooling flows, independently inferred from the ASCA spectra and ROSAT images, exhibit reasonable agreement, providing support for the basic cooling flow picture. We have discussed the systematic uncertainties associated with the results, which are present at the factor ~ 2 level, and commented on the possible effects of intermittent heating in the cooling flows.

(iii) The ASCA spectra for the central regions of the Virgo and Centaurus clusters place firm constraints on the abundances of iron, magnesium, silicon and sulphur in the ICM. Our results firmly favour enrichment models in which a high mass fraction $(70 - 80$ per cent) of the iron in the ICM in the central regions of these clusters (in which strong metallicity gradients are observed) is due to Type Ia supernovae.

(iv) We have confirmed the presence of intrinsic X-ray absorption in the ASCA spectra for the clusters using a variety of spectral models. The measured column densities are sensitive to the spectral models used and range (on average) from a few 10^{20} atom cm^{-2} using a simple single-temperature model to a few 10^{21} atom cm^{-2} using our preferred cooling-flow models.

(v) We have reported detections of 60 and $100\mu m$ infrared emission, coincident with the X-ray centroids, from a number of the systems studied (confirming the original detections by Wise *et al.* 1993 and Cox *et al.* 1995). For the Centaurus Cluster and Abell 2199, the coadded IRAS scan data show that the infrared emission is spatially extended. The infrared fluxes and flux limits are in good agreement with the predicted values due to reprocessed X-ray emission from the intrinsic X-ray absorbing material in the cooling flows.

(vi) We have discussed three methods which may be used to measure the ages of cooling flows from the X-ray data. The application of these techniques to the present sample of objects indicates cooling-flow ages of between 2.5 and 7 Gyr. If the ages of cooling flows in the most massive clusters clusters are primarily set by subcluster merger events, then our results suggest that mergers with subclusters with masses of ~ 30 per cent of the final cluster mass are sufficient to disrupt cooling flows.

ACKNOWLEDGEMENTS

REFERENCES

Allen S.W., 1995, MNRAS, 276, 947
Allen S.W., 1998, MNRAS, 296, 392
Allen S.W., 2000, MNRAS, 315, 269
Allen S.W., Fabian A.C., 1994, MNRAS, 269, 409
Allen S.W., Fabian A.C., 1997, MNRAS, 286, 583
Allen S.W., Fabian A.C., 1998, MNRAS, 297, L63
Allen S.W., Di Matteo T., Fabian A.C., 2000, MNRAS, 311, 493
Akritas M.G., Bershady M.A., 1996, ApJ, 470, 706
Anders E., Grevesse N., 1989, Geochemica et Cosmochimica Acta 53, 197
Arnaud, K.A., 1988, in Fabian A.C., ed., Cooling flows in clusters and galaxies, Kluwer, Dordrecht, p. 31
Arnaud, K.A., 1996, in Astronomical Data Analysis Software and Systems V, eds. Jacoby G. and Barnes J., ASP Conf. Series volume 101, p17
Arnaud K.A., Mushotzky R.F., 1998, ApJ, 501, 119
Bailey M.E., 1980, MNRAS, 191, 195

Balucinska-Church M., McCammon D., 1992, ApJ, 400, 699
Binney J., Tremaine S., 1987, Galactic Dynamics, Princeton Univ. Press, Princeton
Buote D.A., Canizares C.R., Fabian A.C., 1999, MNRAS, 310, 483
Cardiel N., Gorgas J., Aragon-Salamanca A., 1995, MNRAS, 277, 502
Cardiel N., Gorgas J., Aragon-Salamanca A., 1998, MNRAS, 298, 977
Cavaliere A., Menci N., Tozzi P., 1999, MNRAS, 308, 599
Cox C.V., Bregman J.N., Schombert J.M., 1995, ApJS, 99, 405
Crawford C.S., Allen S.W., Ebeling H., Edge A.C., Fabian A.C., 1999, MNRAS, 306, 857
Daines S.J., Fabian A.C., Thomas, P.A., 1994, MNRAS, 268, 1060
David L.P., Harnden F.R., Kearns K.E., Zombeck M.V., 1996, The ROSAT HRI Calibration Report, $ftp : //legacy.gsfc.nasa.gov/rosat/doc/hri/hri\_report$
Dickey J.M., Lockman F.J., 1990, ARA&A, 28, 215
Di Matteo T., Quataert E., Allen S.W., Narayan R., Fabian A.C., 1999, MNRAS, 311, 507
Dotani T. *et al.* , 1996, ASCA News, 4, 3
Dupke R., White R., 2000a, ApJ, 528, 139
Dupke R., White R., 2000b, ApJ, 537, 123
Edge A.C., Stewart G.C., Fabian A.C., 1992, MNRAS, 258, 177
Ezawa H., Fukazawa Y., Makishima K., Ohashi T., Takahara F., Xu H., Yamasaki N.Y., 1997, ApJ, 490, L33
Fabian A.C., 1994, A&AR, 32, 277
Fabian A.C., Crawford C.S., 1990, MNRAS, 247, 439
Fabian A.C., Johnstone R.M., Daines S.J., 1994a, MNRAS, 271, 737
Fabian A.C., Hu E.M., Cowie L.L., Grindlay J., 1981, ApJ, 248, 47
Fabian A.C., Arnaud K.A., Bautz M.W., Tawara Y., 1994b, ApJ, 436, L63
Ferland G.J., Fabian A.C., Johnstone R.M., 2000, MNRAS, submitted
Finoguenov A., Ponman T.J., 1999, MNRAS, 305, 325
Fusco-Femiano R., Dal Fiume, D., Feretti L., Giovannini G., Grandi P., Matt G., Molendi S., Santangelo A., 1999, ApJ, 513, L21
Fukazawa Y. *et al.* 1994, PASJ, 46, L55
Gibson B.K., Loewenstein M., Mushotzky R.F., 1997, MNRAS, 290, 623
Hatsukade I., Kawarabata K., Takenada K., Ishizaka J., 1997, in Makino F., Mitsuda K., eds., X-ray Imaging and Spectroscopy of Cosmic Hot Plasmas, Universal Academy Press, Tokyo, p. 105
Helou G., Khan I.R., Malek L., Boehmer L., 1988, ApJS, 68, 151
Henkel C., Wiklind T., 1997, SSRv, 81, 1
Honda H., Hirayama M., Watanabe M., Kunieda H., Tawara Y., Yamashita K., Ohashi T., Hughes J.P., Henry J.P., 1996, ApJ, 473, L71
Hwang U., Mushotzky R.F., Burns J.O., Fukazawa Y., White R.A., 1999, ApJ, 516, 604
Ikebe Y., Makishima K., Fukazawa Y., Tamura T., Xu H., Ohashi T., Matsushita K., 1999, ApJ, 525, 58
Ishimaru Y., Arimoto N., 1997, PASJ, 49, 1
Johnstone R.M., Fabian A.C., Nulsen P.E.J., 1987, MNRAS, 224, 75
Johnstone R.M., Fabian A.C., Edge A.C., Thomas P.A., 1992, MNRAS, 255, 431
Johnstone R.M., Fabian A.C., Taylor G.B., 1998, MNRAS, 298, 854
Kaastra J.S., Mewe R., 1993, Legacy, 3, HEASARC, NASA
Lacey C., Cole S., 1993, MNRAS, 262, 627
Liedhal D.A., Osterheld A.L., Goldstein W.H., 1995, ApJ, 438, L115
Makishima K., 1997, in Makino F., Mitsuda K., eds., X-ray

Imaging and Spectroscopy of Cosmic Hot Plasmas, Universal Academy Press, Tokyo, p. 137

Markevitch M., Forman W.R., Sarazin C.L., Vikhlinin A., 1998, ApJ, 503, 77

Markevitch M., Vikhlinin A., Forman W.R., Sarazin C.L., 1999, ApJ, 527, 545

Matsumoto H., Koyama K., Awaki H., Tomida H., Tsuru T., Mushotzky R., Hatsukade I., 1996, PASJ, 48, 201

Matsuzawa H., Matsuoka M., Ikebe Y., Mihara T., Yamashita K., 1996, PASJ, 48, 565

McGlynn T.A., Fabian A.C., 1984, MNRAS, 208, 709

McNamara B.R., O'Connell R.W., 1989, AJ, 98, 2018

Mushotzky R.F., Lowenstein M., Arnaud K.A., Tamura T., Fukazawa Y., Matsushita K., Kikuchi K., Hatsukade I., 1996, 466, 686

Nagataki S., Sato K., 1998, ApJ, 504, 629

Nandra K., George I.M., Mushotzky R.F., Turner T.J., Yaqoob T., 1997, ApJ, 477, 602

Navarro J.F., Frenk C.S., White S.D.M., 1995, MNRAS, 275, 720

Nulsen P.E.J., 1986, MNRAS, 221, 377

Nulsen P.E.J., 1998, MNRAS, 297, 1109

Nulsen P.E.J., Böhringer H., 1995, MNRAS, 274, 1093

Nulsen P.E.J., Stewart G.C., Fabian A.C., 1984, MNRAS, 208, 185

O'Dea C.P., Baum S.A., 1996, in Cold gas at high redshift, eds. Bremer M.N., van der Werf P.P., Röttgering H.J.A., Carilli C.L., Kluwer, Dordrecht, p.199

O'Dea C.P., Baum S.A., Maloney P.R., Tacconi L.J., Sparks W.B., 1994, ApJ, 422, 467

Ohashi T., Honda H., Ezawa H., Kikuchi K., 1997, in Makino F., Mitsuda K., eds., X-ray Imaging and Spectroscopy of Cosmic Hot Plasmas, Universal Academy Press, Tokyo, p. 49

Owen F.N., Eilek J.A., 1998, ApJ, 493, 730

Orr A., Yaqoob T., Parmar A.N., Piro L., White N.E., Grandi P., A&A, 337, 685

Pedlar A., Ghataure H.S., Davies R.D., Harrison B.A., Perley R., Crane P.C., Unger S.W., 1990, MNRAS, 246, 477

Peres C.B., Fabian A.C., Edge A.C., Allen S.W., Johnstone R.M., White D.A., 1998, MNRAS, 298, 416

Raymond J.C., Smith B.W., 1977, ApJS, 35, 419

Reisenegger A., Miralda-Escudé J., Waxman E., 1996, ApJ, 457, 11L

Rephaeli Y., Gruber D., Blanco P., 1999, ApJ, 511, 21L

Roettiger K., Burns J.O., Loken C., 1996, ApJ, 473, 651

Schindler S., 1996, A&A, 305, 756

Stark A.A., Gammie C.F., Wilson R.W., Bally J., Linke R.A., Heiles C. & Hurwitz M., 1992. ApJS, 79, 77

Tamura T. *et al.* , 1996, PASJ, 48, 671

Tanaka Y., Inoue H., Holt S.S., 1994, PASJ, 46, L37

Taylor G.B., Barton E.J., Ge J., 1994, AJ, 107, 1942

Taylor G.B., Allen S.W., Fabian A.C., 1999, in Diffuse Thermal and Relativistic Plasma in Galaxy Clusters, eds. Böhringer H., Feretti L., Schuecker P., MPE Report 271

Thomas P.A., Fabian A.C., Nulsen P.E.J, 1987, MNRAS, 228, 973

Tucker W., David L.P., ApJ, 1997, 484, 602

Voit G.M., Donahue M., 1995, ApJ, 452, 164

Watanabe M., Yamashita K., Kunieda H., Tawara Y., 1997, in Makino F., Mitsuda K., eds., X-ray Imaging and Spectroscopy of Cosmic Hot Plasmas, Universal Academy Press, Tokyo, p. 131

White D.A., Jones C., Forman W., 1997, MNRAS, 292, 419

White D.A., Fabian A.C., Johnstone R.M., Mushotzky R.F., Arnaud K.A., 1991, MNRAS, 252, 72

Wise M.W., O'Connell R.W., Bregman J.N., Roberts M.S., 1993, ApJ, 405, 94

Wise M.W., Sarazin C.L., 2000, ApJ, submitted

Xu H., Makishima K., Fukazawa Y., Ikebe Y., Kikuchi K., Ohashi T., Tamura T., 1998, ApJ, 500, 738

Table 1. Summary of the ASCA Observations. Column 2 lists the optically-determined redshifts for the clusters (for the Virgo Cluster we assume a distance of 18 Mpc). Column 3 summarizes the dates of the observations. Columns $4 - 7$ list the net exposure times (in seconds) in each of the four detectors after all screening and cleaning procedures were carried out.

Cluster	z	Date	S0	S1	G2	G3
Abell 426	0.0183	1993 Aug 06	13910	6814	15618	14916
Abell 496	0.0320	1993 Sep 21	29685	21515	40050	39986
Virgo	18Mpc	1993 Jun 07	13633	14668	16874	16874
Centaurus	0.0104	1995 May 19	68820	67650	70981	70999
Coma	0.0232	1993 Jun 14	8732	6637	9312	9312
Abell 1795	0.0634	1993 Jun 16	31284	——	37649	37641
Abell 2199	0.0309	1993 Jul 25	19153	13932	29758	29758
Abell 2597	0.0852	1996 Dec 06	33933	34697	39249	39239

Table 2. The radii of the circular extraction regions used in the analysis of the ASCA SIS data (in arcmin and kpc) and the chip modes used in the observations (either 1,2 or 4-CCD mode). The numbers in parentheses indicate the number of chips contributing to the extracted spectra. For the GIS data a fixed extraction radius of 6 arcmin was used.

Cluster	S0 (amin/kpc)	S1 (amin/kpc)	SIS Chip Mode
Abell 426	4.9/152	4.7/145	4(1)
Abell 496	3.9/206	3.2/169	4(1)
Virgo	4.9/25.5	4.1/21.3	4(2)
Centaurus	—	3.7/66.0	1(1)
Coma	10.0/389	9.5/370	4(4)
Abell 1795	4.5/447	—	4(2)
Abell 2199	5.3/271	4.2/215	4(2)
Abell 2597	4.5/580	3.7/477	2(2)

Table 3. Summary of the ROSAT Observations. Columns 2 and 3 list the dates of the observations and the instrument used. Column 4 lists the exposure times (in seconds). Where more than a single observation of a cluster was made, details for each observation are given. Columns 5 and 6 list the coordinates for the centroids of the X-ray emission from the clusters.

Cluster	Date	Instrument	Exposure	R.A. (J2000).	Dec. (J2000.)
Abell 426	1992 Feb 02	PSPC	4787	$03^{\rm h}19^{\rm m}48.5^{\rm s}$	$41°30'27''$
Abell 496	1992 Sep 12	HRI	14488	$04^{\rm h}33^{\rm m}38.1^{\rm s}$	$-13°15'42''$
Virgo	1992 Dec 17	PSPC	9961	$12^{\rm h}30^{\rm m}49.8^{\rm s}$	$12°23'32''$
Centaurus	1994 Jul 05	PSPC	3192	$12^{\rm h}48^{\rm m}48.7^{\rm s}$	$-41°18'44''$
Coma	1991 Jun 17	PSPC	22108	$12^{\rm h}59^{\rm m}46.1^{\rm s}$	$27°56'21''$
Abell 1795 #1	1992 Jun 25	HRI	2768	$13^{\rm h}48^{\rm m}52.7^{\rm s}$	$26°35'27''$
Abell 1795 #2	1993 Jan 21	HRI	11088	—	—
Abell 1795 #3	1994 Jun 23	HRI	11080	—	—
Abell 2199 #1	1991 Feb 10	HRI	5308	$16^{\rm h}28^{\rm m}38.5^{\rm s}$	$39°33'03''$
Abell 2199 #2	1994 Feb 03	HRI	26528	—	—
Abell 2199 #3	1994 Aug 31	HRI	20976	—	—
Abell 2597	1992 Jun 06	HRI	16228	$23^{\rm h}25^{\rm m}19.7^{\rm s}$	$-12°07'27''$

Table 4. The best-fit parameter values and 90 per cent ($\Delta\chi^2 = 2.71$) confidence limits from the basic spectral analysis of the ASCA data. Temperatures (kT), metallicities (Z), column densities (N_H), intrinsic column densities (ΔN_H), mass deposition rates ($\dot{M}_S$) and the normalization of the intrinsically absorbed (cooler) emission components in spectral model D, were linked to take the same values in all four detectors. Only the normalization of the hotter isothermal emission component was allowed to vary independently for each detector. Temperatures are quoted in keV and metallicities as a fraction of the solar photospheric value (Anders & Grevesse 1989). Column densities and intrinsic column densities are in units of 10^{21} atom cm^{-2}. Mass deposition rates are in $M_\odot$ yr^{-1}.

	Parameters	Model A	Model B	Model C	Model D	Model E
	kT	$4.22^{+0.03}_{-0.03}$	$4.31^{+0.04}_{-0.04}$	$4.70^{+0.18}_{-0.13}$	$6.00^{+0.27}_{-0.29}$	$4.57^{+0.09}_{-0.08}$
	Z	$0.47^{+0.02}_{-0.02}$	$0.47^{+0.01}_{-0.02}$	$0.46^{+0.02}_{-0.02}$	$0.45^{+0.02}_{-0.02}$	$0.46^{+0.02}_{-0.02}$
Abell 426	N_H	1.49	$1.37^{+0.03}_{-0.03}$	$1.14^{+0.10}_{-0.15}$	$0.83^{+0.12}_{-0.10}$	$0.93^{+0.16}_{-0.19}$
	$\dot{M}$	—	—	258^{+89}_{-89}	—	303^{+75}_{-74}
	kT_2	—	—	—	$2.17^{+0.14}_{-0.16}$	—
	ΔN_H	—	—	$3.6^{+0.4}_{-0.5}$	$2.5^{+0.5}_{-0.4}$	$3.4^{+0.4}_{-0.4}$
	χ^2/DOF	2487/1659	2443/1658	2405/1656	2229/1655	2389/1656
	kT	$3.78^{+0.04}_{-0.04}$	$3.54^{+0.05}_{-0.05}$	$3.86^{+0.15}_{-0.15}$	$3.85^{+0.10}_{-0.08}$	$3.67^{+0.08}_{-0.07}$
	Z	$0.50^{+0.03}_{-0.03}$	$0.51^{+0.03}_{-0.03}$	$0.50^{+0.04}_{-0.03}$	$0.50^{+0.03}_{-0.03}$	$0.50^{+0.03}_{-0.03}$
Abell 496	N_H	0.46	$0.83^{+0.05}_{-0.05}$	$0.49^{+0.21}_{-0.21}$	$0.74^{+0.08}_{-0.07}$	$0.44^{+0.22}_{-0.24}$
	$\dot{M}$	—	—	136^{+46}_{-55}	—	110^{+39}_{-42}
	kT_2	—	—	—	$0.47^{+0.08}_{-0.08}$	—
	ΔN_H	—	—	$4.3^{+0.6}_{-0.9}$	$11.9^{+2.0}_{-1.5}$	$3.6^{+0.6}_{-0.7}$
	χ^2/DOF	1546/1283	1400/1282	1379/1280	1319/1279	1380/1280
	kT	$2.05^{+0.01}_{-0.02}$	$2.02^{+0.01}_{-0.02}$	$2.23^{+0.03}_{-0.03}$	$2.19^{+0.02}_{-0.03}$	$2.08^{+0.02}_{-0.02}$
	Z	$0.67^{+0.02}_{-0.02}$	$0.65^{+0.02}_{-0.02}$	$0.80^{+0.03}_{-0.03}$	$0.79^{+0.04}_{-0.03}$	$0.75^{+0.02}_{-0.03}$
Virgo	N_H	0.25	$0.35^{+0.04}_{-0.03}$	$0.05^{+0.15}_{-0.05}$	$0.31^{+0.07}_{-0.07}$	$0.37^{+0.19}_{-0.18}$
	$\dot{M}$	—	—	$10.7^{+1.0}_{-1.4}$	—	$5.8^{+1.0}_{-0.9}$
	kT_2	—	—	—	$0.84^{+0.04}_{-0.03}$	—
	ΔN_H	—	—	$3.76^{+0.28}_{-0.48}$	$5.0^{+0.6}_{-0.8}$	$1.88^{+0.53}_{-0.65}$
	χ^2/DOF	2527/1153	2502/1152	1975/1150	1950/1149	2018/1150
	kT	$2.77^{+0.01}_{-0.02}$	$2.70^{+0.01}_{-0.02}$	$3.20^{+0.07}_{-0.07}$	$3.24^{+0.08}_{-0.08}$	$2.92^{+0.03}_{-0.03}$
	Z	$1.18^{+0.03}_{-0.03}$	$1.16^{+0.02}_{-0.03}$	$1.24^{+0.03}_{-0.03}$	$0.93^{+0.04}_{-0.03}$	$1.23^{+0.03}_{-0.03}$
Centaurus	N_H	0.81	$1.01^{+0.03}_{-0.03}$	$1.00^{+0.20}_{-0.20}$	$1.28^{+0.08}_{-0.10}$	$1.01^{+0.21}_{-0.16}$
	$\dot{M}$	—	—	$42.0^{+3.7}_{-3.7}$	—	$36.3^{+2.4}_{-2.8}$
	kT_2	—	—	—	$1.34^{+0.04}_{-0.04}$	—
	ΔN_H	—	—	$2.46^{+0.36}_{-0.38}$	$0.23^{+0.35}_{-0.23}$	$1.92^{+0.25}_{-0.33}$
	χ^2/DOF	4928/1553	4782/1552	2703/1549	2584/1549	2696/1549

Table 4. Spectral Results - continued

	Parameters	Model A	Model B	Model C	Model D	Model E
Coma	kT	$6.44^{+0.58}_{-0.52}$	$8.08^{+0.26}_{-0.25}$	—	$9.07^{+0.62}_{-0.89}$	—
	Z	$0.20^{+0.07}_{-0.08}$	$0.19^{+0.04}_{-0.02}$	—	$0.21^{+0.04}_{-0.04}$	—
	N_{H}	0.09	$0.24^{+0.05}_{-0.05}$	—	$0.11^{+0.07}_{-0.07}$	—
	$\dot{M}$	—	—	—	—	—
	kT_2	—	—	—	< 0.87	—
	ΔN_{H}	—	—	—	> 10.7	—
	χ^2/DOF	1696/1228	1274/1227	—	1254/1224	—
Abell 1795	kT	$5.40^{+0.08}_{-0.09}$	$5.33^{+0.10}_{-0.11}$	$5.87^{+0.25}_{-0.19}$	$6.21^{+0.25}_{-0.22}$	$5.61^{+0.17}_{-0.15}$
	Z	$0.36^{+0.03}_{-0.02}$	$0.36^{+0.03}_{-0.02}$	$0.37^{+0.02}_{-0.03}$	$0.37^{+0.03}_{-0.03}$	$0.37^{+0.02}_{-0.03}$
	N_{H}	0.12	$0.17^{+0.05}_{-0.05}$	$0.00^{+0.06}_{-0.00}$	$0.00^{+0.03}_{-0.00}$	$0.00^{+0.06}_{-0.00}$
	$\dot{M}$	—	—	301^{+76}_{-76}	—	246^{+71}_{-70}
	kT_2	—	—	—	$1.48^{+0.54}_{-0.29}$	—
	ΔN_{H}	—	—	$3.1^{+0.7}_{-0.5}$	$5.2^{+2.8}_{-2.9}$	$2.6^{+0.7}_{-0.5}$
	χ^2/DOF	1442/1236	1440/1235	1419/1233	1387/1232	1422/1233
Abell 2199	kT	$4.16^{+0.05}_{-0.05}$	$3.91^{+0.06}_{-0.05}$	$4.38^{+0.12}_{-0.22}$	$4.97^{+0.35}_{-0.25}$	$4.09^{+0.08}_{-0.09}$
	Z	$0.42^{+0.02}_{-0.02}$	$0.43^{+0.02}_{-0.03}$	$0.43^{+0.03}_{-0.03}$	$0.40^{+0.03}_{-0.03}$	$0.42^{+0.03}_{-0.03}$
	N_{H}	0.09	$0.40^{+0.05}_{-0.05}$	$0.00^{+0.25}_{-0.00}$	$0.00^{+0.10}_{-0.00}$	$0.00^{+0.19}_{-0.00}$
	$\dot{M}$	—	—	180^{+22}_{-76}	—	147^{+20}_{-46}
	kT_2	—	—	—	$1.84^{+0.36}_{-0.28}$	—
	ΔN_{H}	—	—	$4.1^{+0.5}_{-0.9}$	$2.8^{+1.6}_{-1.1}$	$3.5^{+0.5}_{-0.7}$
	χ^2/DOF	1693/1295	1571/1294	1550/1292	1516/1291	1549/1292
Abell 2597	kT	$3.90^{+0.07}_{-0.06}$	$3.38^{+0.06}_{-0.07}$	$3.88^{+0.29}_{-0.30}$	$2.31^{+0.23}_{-0.28}$	$3.45^{+0.11}_{-0.10}$
	Z	$0.32^{+0.03}_{-0.03}$	$0.35^{+0.03}_{-0.04}$	$0.36^{+0.05}_{-0.04}$	$0.29^{+0.04}_{-0.04}$	$0.35^{+0.04}_{-0.04}$
	N_{H}	0.25	$0.99^{+0.07}_{-0.08}$	$0.21^{+0.44}_{-0.21}$	$0.65^{+0.55}_{-0.28}$	$0.00^{+0.38}_{-0.00}$
	$\dot{M}$	—	—	774^{+169}_{-332}	—	717^{+66}_{-208}
	kT_2	—	—	—	$6.22^{+1.86}_{-1.23}$	—
	ΔN_{H}	—	—	$5.4^{+0.9}_{-0.9}$	$2.4^{+1.7}_{-2.4}$	$5.0^{+0.7}_{-0.7}$
	χ^2/DOF	1412/984	1127/983	1114/981	1083/980	1110/981

Table 5. The mass deposition rates (in $M_\odot \, yr^{-1}$) and intrinsic column densities (in units of 10^{21} atom cm^{-2}) determined from the fits to the ASCA spectra with the isothermal cooling flow models for various values of the slope parameter η.

	Parameters	$\eta = 0.75$	$\eta = 1.0$	$\eta = 1.5$	$\eta = 2.0$	$\eta = 2.5$
Abell 426	$\dot{M}$	283^{+68}_{-74}	303^{+75}_{-74}	329^{+81}_{-83}	340^{+89}_{-83}	347^{+95}_{-83}
	ΔN_H	$3.2^{+0.3}_{-0.4}$	$3.4^{+0.4}_{-0.4}$	$3.7^{+0.3}_{-0.4}$	$3.8^{+0.4}_{-0.4}$	$3.9^{+0.4}_{-0.4}$
	χ^2/DOF	2391.1/1656	2388.9/1656	2389.8/1656	2390.5/1655	2390.7/1656
Abell 496	$\dot{M}$	$93.3^{+37.6}_{-37.2}$	110^{+39}_{-42}	136^{+46}_{-50}	152^{+50}_{-54}	162^{+52}_{-57}
	ΔN_H	$3.2^{+0.6}_{-0.7}$	$3.6^{+0.6}_{-0.7}$	$4.0^{+0.6}_{-0.7}$	$4.2^{+0.6}_{-0.7}$	$4.4^{+0.6}_{-0.7}$
	χ^2/DOF	1382.7/1280	1379.9/1280	1377.5/1280	1376.2/1280	1375.4/1280
Virgo	$\dot{M}$	$5.0^{+0.8}_{-0.9}$	$5.8^{+1.0}_{-0.9}$	$7.9^{+1.1}_{-1.2}$	$9.2^{+1.3}_{-1.4}$	$10.1^{+1.4}_{-1.5}$
	ΔN_H	$1.4^{+0.5}_{-0.7}$	$1.9^{+0.5}_{-0.7}$	$2.7^{+0.5}_{-0.6}$	$3.1^{+0.4}_{-0.5}$	$3.3^{+0.4}_{-0.5}$
	χ^2/DOF	2022.9/1150	2017.9/1150	2004.0/1150	1996.3/1150	1991.5/1150
Centaurus	$\dot{M}$	$33.3^{+2.6}_{-2.0}$	$36.3^{+2.4}_{-2.8}$	$41.7^{+3.2}_{-3.2}$	$45.3^{+3.6}_{-3.6}$	$47.7^{+3.9}_{-3.8}$
	ΔN_H	$1.7^{+0.2}_{-0.3}$	$1.9^{+0.3}_{-0.3}$	$2.3^{+0.3}_{-0.3}$	$2.6^{+0.3}_{-0.3}$	$2.7^{+0.3}_{-0.3}$
	χ^2/DOF	2708.4/1549	2696.3/1549	2681.6/1549	2678.2/1549	2678.0/1549
Abell 1795	$\dot{M}$	222^{+69}_{-67}	246^{+71}_{-70}	284^{+77}_{-77}	306^{+186}_{-80}	321^{+83}_{-83}
	ΔN_H	$2.3^{+0.7}_{-0.4}$	$2.6^{+0.7}_{-0.5}$	$2.9^{+0.7}_{-0.5}$	$3.0^{+0.8}_{-0.5}$	$3.2^{+0.7}_{-0.5}$
	χ^2/DOF	1422.7/1233	1421.5/1233	1420.3/1233	1419.6/1233	1419.2/1233
Abell 2199	$\dot{M}$	125^{+17}_{-40}	147^{+20}_{-46}	168^{+22}_{-54}	186^{+23}_{-59}	197^{+24}_{-64}
	ΔN_H	$3.2^{+0.5}_{-0.7}$	$3.5^{+0.5}_{-0.7}$	$3.8^{+0.5}_{-0.6}$	$4.0^{+0.5}_{-0.7}$	$4.2^{+0.5}_{-0.7}$
	χ^2/DOF	1550.1/1292	1548.7/1292	1547.6/1292	1547.1/1292	1546.8/1292
Abell 2597	$\dot{M}$	613^{+59}_{-186}	717^{+66}_{-208}	867^{+77}_{-247}	963^{+85}_{-277}	1029^{+91}_{-299}
	ΔN_H	$4.7^{+0.7}_{-0.6}$	$5.0^{+0.7}_{-0.7}$	$5.4^{+0.7}_{-0.7}$	$5.6^{+0.7}_{-0.7}$	$5.7^{+0.7}_{-0.6}$
	χ^2/DOF	1112.2/981	1110.2/981	1108.4/981	1107.5/981	1106.9/981

Table 6. The results from the fits to individual SIS data sets (instrument specified in parentheses) over the $3.0 - 10.0$ keV energy range, using spectral model A.

Cluster	kT (keV)	Z ($Z_\odot$)	χ^2/DOF
Abell 426 (S1)	$5.77^{+0.46}_{-0.41}$	$0.46^{+0.07}_{-0.06}$	148.1/143
Abell 496 (S0)	$4.14^{+0.38}_{-0.34}$	$0.35^{+0.07}_{-0.07}$	117.7/118
Virgo (S0)	$2.17^{+0.11}_{-0.11}$	$0.51^{+0.10}_{-0.09}$	108.5/108
Centaurus (S1)	$3.18^{+0.18}_{-0.16}$	$0.97^{+0.13}_{-0.11}$	146.5/142
Coma (S0)	$8.48^{+1.04}_{-0.85}$	$0.17^{+0.06}_{-0.06}$	146.7/149
Abell 1795 (S0)	$6.10^{+0.49}_{-0.43}$	$0.38^{+0.06}_{-0.05}$	165.0/146
Abell 2199 (S0)	$4.80^{+0.42}_{-0.37}$	$0.40^{+0.07}_{-0.07}$	153.3/126
Abell 2597 (S1)	$4.05^{+0.66}_{-0.53}$	$0.34^{+0.13}_{-0.11}$	67.6/78

Table 7. The best-fit parameter values and 90 per cent ($\Delta\chi^2 = 2.71$) confidence limits from the spectral analysis with the two temperature model incorporating the power-law components. The normalizations of the power-law components (A_1) are quoted at an energy of 1keV in units of 10^{-5} photon keV^{-1}cm^{-2}s^{-1}. The $2 - 10$ keV fluxes associated with the power-law components ($F_{X,2-10}$) are in units of $\mathrm{erg\,cm^{-2}\,s^{-1}}$ and are not corrected for absorption. The intrinsic luminosities in the $1 - 10$ keV band ($L_{X,1-10}$) are corrected for absorption and are in units of $\mathrm{erg\,s^{-1}}$. $\Delta\chi^2$ values are the improvements in χ^2 obtained with the introduction of the power-law component into the best-fitting two-temperature model (model D; or in the case of the Coma Cluster the best fitting single temperature model B). The final χ^2 values and number of degrees of freedom in the fits are also listed (χ^2/DOF). The results for the Virgo and Centaurus clusters are from Allen *et al.* (2000). For these two systems the two temperature models incorporating variable element abundances (Section 4) were used in the analyses.

Parameters	Abell 426	Abell 496	Virgo	Centaurus
kT	$4.43^{+0.35}_{-0.27}$	$3.42^{+0.12}_{-0.12}$	$2.01^{+0.04}_{-0.03}$	$3.27^{+0.26}_{-0.12}$
Z	$0.78^{+0.08}_{-0.07}$	$0.53^{+0.06}_{-0.03}$	$0.72^{+0.04}_{-0.04}$	$0.86^{+0.03}_{-0.07}$
N_H	$0.43^{+0.19}_{-0.23}$	$0.64^{+0.10}_{-0.16}$	$0.30^{+0.08}_{-0.08}$	$0.96^{+0.22}_{-0.26}$
$\dot{M}$	—	—	—	—
kT_2	$2.14^{+0.45}_{-0.42}$	$0.50^{+0.12}_{-0.10}$	$0.79^{+0.05}_{-0.05}$	$1.46^{+0.07}_{-0.06}$
ΔN_H	$3.3^{+0.5}_{-0.4}$	$12.3^{+2.8}_{-1.7}$	$4.88^{+0.72}_{-0.86}$	$0.59^{+1.01}_{-0.54}$
Γ	$2.05^{+0.05}_{-0.05}$	$1.44^{+0.44}_{-0.38}$	$1.40^{+0.37}_{-0.46}$	$0.76^{+0.59}_{-0.65}$
A_1	7878^{+1007}_{-1061}	100^{+150}_{-56}	137^{+159}_{-55}	$22.0^{+62.1}_{-16.4}$
$F_{X,2-10}$	$1.80^{+0.12}_{-0.14} \times 10^{-10}$	$5.58^{+1.42}_{-1.00} \times 10^{-12}$	$8.69^{+1.70}_{-1.56} \times 10^{-12}$	$4.20^{+1.29}_{-0.99} \times 10^{-12}$
$L_{X,1-10}$	$3.96^{+0.34}_{-0.36} \times 10^{44}$	$3.29^{+1.49}_{-0.84} \times 10^{43}$	$4.22^{+1.37}_{-1.06} \times 10^{41}$	$2.14^{+0.99}_{-0.60} \times 10^{42}$
$\Delta\chi^2$	171	49.7	90.0	38.8
χ^2/DOF	2058/1653	1269/1277	1468/1143	954.7/746

Parameters	Abell 1795	Abell 2199	Abell 2597	Coma
kT	$5.50^{+0.51}_{-0.88}$	$3.64^{+1.11}_{-0.19}$	$3.06^{+0.25}_{-0.22}$	$8.46^{+0.63}_{-0.48}$
Z	$0.36^{+0.04}_{-0.03}$	$0.44^{+0.04}_{-0.06}$	$0.45^{+0.09}_{-0.09}$	$0.20^{+0.06}_{-0.04}$
N_H	$0.00^{+0.09}_{-0.00}$	$0.27^{+0.15}_{-0.27}$	$0.36^{+0.35}_{-0.36}$	$0.54^{+0.28}_{-0.24}$
$\dot{M}$	—	—	—	—
kT_2	$1.38^{+0.46}_{-0.45}$	$0.91^{+0.39}_{-0.46}$	$0.86^{+0.16}_{-0.11}$	—
ΔN_H	$7.2^{+5.7}_{-3.3}$	$10.8^{+6.7}_{-3.8}$	$12.4^{+4.1}_{-1.7}$	—
Γ	$0.12^{+0.98}_{-2.05}$	$1.01^{+0.78}_{-1.61}$	$1.80^{+0.42}_{-0.66}$	$3.34^{+0.82}_{-1.63}$
A_1	$5.96^{+80.0}_{-5.92}$	$62.3^{+239}_{-61.6}$	133^{+187}_{-102}	310^{+191}_{-170}
$F_{X,2-10}$	$3.53^{+5.51}_{-2.20} \times 10^{-12}$	$7.24^{+3.02}_{-5.65} \times 10^{-12}$	$4.21^{+1.25}_{-1.40} \times 10^{-12}$	$1.28^{+17.5}_{-0.80} \times 10^{-12}$
$L_{X,1-10}$	$5.96^{+12.45}_{-4.10} \times 10^{43}$	$3.52^{+2.74}_{-1.00} \times 10^{43}$	$1.99^{+1.11}_{-0.92} \times 10^{44}$	$8.49^{+48.6}_{-3.78} \times 10^{42}$
$\Delta\chi^2$	10.8	7.3	32.2	9.4
χ^2/DOF	1376/1230	1509/1289	1051/978	1265/1225

Table 8. The results on the individual element abundances in the central regions of the Virgo and Centaurus clusters using the two-temperature model with free-fitting element abundances (see Section 5). Error bars are the 90 per cent confidence limits ($\Delta\chi^2 = 2.71$) on a single interesting parameter. The abundances of elements not listed in the table were linked to have the same ratios relative to their solar values as that of Fe.

Parameter	Virgo	Centaurus
kT	$2.13^{+0.04}_{-0.04}$	$4.09^{+0.61}_{-0.59}$
$N_{\rm H}$	$0.33^{+0.08}_{-0.08}$	$0.85^{+0.24}_{-0.22}$
$\Delta N_{\rm H}$	$3.41^{+0.96}_{-1.23}$	$0.62^{+0.74}_{-0.62}$
kT_2	$0.86^{+0.06}_{-0.05}$	$1.55^{+0.09}_{-0.11}$
Fe	$0.79^{+0.05}_{-0.04}$	$0.93^{+0.05}_{-0.04}$
Mg	$0.28^{+0.11}_{-0.10}$	$0.30^{+0.20}_{-0.15}$
Si	$1.20^{+0.09}_{-0.09}$	$1.29^{+0.19}_{-0.14}$
Na	$11.0^{+3.4}_{-3.2}$	—
S	$1.00^{+0.10}_{-0.09}$	$1.25^{+0.24}_{-0.16}$
O	—	$0.00^{+0.06}_{-0.00}$
χ^2/DOF	468.9/357	322.3/216

Table 9. Results from the deprojection analysis of the ROSAT images. Column 2 lists the binsize (in arcsec and kpc) used in the analysis. Columns $3-5$ summarize the velocity dispersions, core radii and galaxy linear mass (GLM) components (where required) used to parameterize the cluster mass profiles. Columns 6-8 summarize the results on the cooling time ($t_{\rm cool}$; the time for the gas in the central bin to cool from the ambient cluster temperature at constant pressure), the cooling radius ($r_{\rm cool}$; the radius where the cooling time of the cluster gas first exceeds a Hubble time) and the mass deposition rates ($\dot{M}_{\rm I}$; the integrated mass deposition rates within the cooling radii). Errors on the velocity dispersions are 90 per cent confidence limits. Errors on the cooling times are the 10 and 90 percentile values from 100 Monte Carlo simulations. The upper and lower confidence limits on the cooling radii are the points where the 10 and 90 percentiles exceed and become less than the Hubble time, respectively. Errors on the mass deposition rates are the 90 and 10 percentile values at the upper and lower limits for the cooling radius. We note that the errors on the deprojection results do not account for uncertainties in the total mass profiles.

Cluster	binsize (arcsec/kpc)	σ ($\rm km\,s^{-1}$)	$r_{\rm c}$ (kpc)	GLM ($\rm M_\odot kpc^{-1}$)	$t_{\rm cool}$ (10^9 yr)	$r_{\rm cool}$ (kpc)	$\dot{M}_{\rm I}$ ($\rm M_\odot\,yr^{-1}$)
				MASS PROFILES		DEPROJECTION RESULTS	
Abell 426	30/15.5	670^{+10}_{-10}	40	—	$0.74^{+0.04}_{-0.04}$	188^{+36}_{-10}	587^{+94}_{-43}
Abell 496	12/10.6	550^{+10}_{-10}	40	8.0×10^{10}	$0.55^{+0.15}_{-0.11}$	126^{+81}_{-17}	111^{+194}_{-44}
Virgo	30/2.60	450^{+10}_{-10}	50	8.0×10^{10}	$0.10^{+0.01}_{-0.01}$	106^{+28}_{-19}	$23.2^{+9.1}_{-5.6}$
Centaurus	30/8.91	430^{+10}_{-10}	35	1.2×10^{11}	$0.44^{+0.03}_{-0.03}$	124^{+41}_{-12}	$39.3^{+25.5}_{-7.8}$
Coma	30/19.4	760^{+30}_{-20}	300	5.0×10^{10}	$14.2^{+8.3}_{-3.8}$	< 29	< 1
Abell 1795	16/26.5	700^{+20}_{-20}	50	1.0×10^{11}	$1.37^{+0.09}_{-0.08}$	191^{+34}_{-19}	462^{+108}_{-56}
Abell 2199	16/13.6	570^{+10}_{-10}	80	1.5×10^{11}	$1.01^{+0.05}_{-0.04}$	173^{+11}_{-30}	197^{+20}_{-41}
Abell 2597	12/25.8	610^{+10}_{-10}	40	—	$0.86^{+0.10}_{-0.08}$	162^{+82}_{-21}	423^{+91}_{-99}

Table 10. A comparison of the integrated mass deposition rates determined from the deprojection analysis, both before correction ($\dot{M}_{\rm I}$) and after correction for the effects of intrinsic absorption due to a uniform screen of cold gas ($\dot{M}_{\rm C}$; Section 7.1), with the values determined from the spectral analysis ($\dot{M}_{\rm S}$) using spectral model E (model C for the Virgo Cluster). Errors on the corrected deprojection results account for the statistical uncertainties in the deprojected quantities but not the errors in the the intrinsic column densities.

Cluster	INTRINSIC ABSORPTION $\Delta N_{\rm H}$ (10^{21} atom cm^{-2})	ORIGINAL DEPROJ. $\dot{M}_{\rm I}$ (M$_\odot$ yr^{-1})	CORRECTED DEPROJ. $\dot{M}_{\rm C}$ (M$_\odot$ yr^{-1})	SPECTRAL ANALYSIS $\dot{M}_{\rm S}$ (M$_\odot$ yr^{-1})
Abell 426	$3.4^{+0.4}_{-0.4}$	587^{+94}_{-43}	1175^{+319}_{-112}	303^{+75}_{-74}
Abell 496	$3.6^{+0.6}_{-0.7}$	111^{+194}_{-44}	289^{+470}_{-208}	110^{+39}_{-42}
Virgo	$3.76^{+0.28}_{-0.48}$	$23.2^{+9.1}_{-5.6}$	$47.5^{+29.6}_{-15.7}$	$10.7^{+1.0}_{-1.4}$
Centaurus	$1.92^{+0.25}_{-0.33}$	$39.3^{+25.5}_{-7.8}$	$71.9^{+22.6}_{-24.6}$	$36.3^{+2.4}_{-2.8}$
Abell 1795	$2.6^{+0.7}_{-0.5}$	462^{+108}_{-56}	1212^{+164}_{-208}	246^{+71}_{-70}
Abell 2199	$3.5^{+0.5}_{-0.7}$	197^{+20}_{-41}	599^{+79}_{-77}	147^{+20}_{-46}
Abell 2597	$5.0^{+0.7}_{-0.7}$	423^{+91}_{-99}	1159^{+268}_{-654}	717^{+66}_{-208}

Table 11. A summary of the results on intrinsic absorption from the ASCA data. Columns $2-6$ list the differences between the spectrally-determined column densities and the nominal Galactic values (in units of 10^{21} atom cm^{-2}) for spectral models B, C, C', D and E. Also listed are the (90 per cent confidence) constraints on the covering fraction of the intrinsic absorber, f, determined using spectral model E. All results assume solar metallicity in the absorbing material. The errors on the mean values are the standard deviations for the sample of cooling-flow clusters (the Coma cluster is excluded).

Cluster	B-A	C-A	C'-A	D-A	E-A	f
Abell 426	$-0.12^{+0.03}_{-0.03}$	$3.6^{+0.4}_{-0.5}$	$-0.11^{+0.05}_{-0.04}$	$2.5^{+0.5}_{-0.4}$	$3.4^{+0.4}_{-0.4}$	> 0.99
Abell 496	$0.37^{+0.05}_{-0.05}$	$4.3^{+0.6}_{-0.9}$	$0.38^{+0.10}_{-0.06}$	$11.9^{+2.0}_{-1.5}$	$3.6^{+0.6}_{-0.7}$	> 0.97
Virgo	$0.10^{+0.04}_{-0.03}$	$3.8^{+0.3}_{-0.5}$	$0.65^{+0.06}_{-0.06}$	$5.0^{+0.6}_{-0.8}$	$1.88^{+0.53}_{-0.65}$	$0.66^{+0.15}_{-0.16}$
Centaurus	$0.20^{+0.03}_{-0.03}$	$2.5^{+0.4}_{-0.4}$	$1.25^{+0.06}_{-0.06}$	$0.23^{+0.35}_{-0.23}$	$1.92^{+0.25}_{-0.33}$	> 0.98
Coma	$0.15^{+0.05}_{-0.05}$	—	—	—	—	—
Abell 1795	$0.05^{+0.05}_{-0.05}$	$3.1^{+0.7}_{-0.5}$	$0.10^{+0.11}_{-0.09}$	$5.2^{+2.8}_{-2.9}$	$2.6^{+0.7}_{-0.5}$	> 0.85
Abell 2199	$0.31^{+0.05}_{-0.05}$	$4.1^{+1.6}_{-0.9}$	$0.39^{+0.09}_{-0.09}$	$2.8^{+1.6}_{-1.1}$	$3.5^{+0.5}_{-0.7}$	> 0.96
Abell 2597	$0.74^{+0.07}_{-0.08}$	$5.4^{+0.9}_{-0.9}$	$0.74^{+0.07}_{-0.08}$	$2.4^{+1.7}_{-2.4}$	$5.0^{+0.7}_{-0.7}$	> 0.98
MEAN	0.24 ± 0.28	3.8 ± 0.9	0.49 ± 0.45	4.3 ± 3.8	3.1 ± 1.1	

Table 12. Column 2 lists the X-ray luminosities expected to be reprocessed into (predominantly) far infrared emission by the intrinsic absorbing material in the clusters. The best-fit parameters determined with spectral model E have been used in the calculations (except for the Virgo cluster, for which model C is preferred). Columns 3 and 4 lists the observed 60 and $100\mu m$ IRAS fluxes within a 4 arcmin (radius) aperture centered on the X-ray centres (Table 3) measured using the IPAC SCANPI software and co-added IRAS scans. Error bars are the root-mean-square deviations in the residuals, external to the source extraction regions, after baseline subtraction. Where no detection was made an upper limit equal to three times the r.m.s. deviation in the residuals is given. Column 5 lists the in-scan separation ΔR (in arcmin) between the peak of the $100\mu m$ emission and the X-ray centre. Column 6 lists the total $1-1000\mu m$ luminosities calculated using equation 2. For Abell 2597, the predicted reprocessed luminosity may be overestimated due to the effects of radiation damage to the SIS detectors (see Section 7.2.)

Cluster	$L_{\rm repro.}$ $(10^{44}~{\rm erg\,s^{-1}})$	S_{60} (mJy)	S_{100} (mJy)	ΔR (arcmin)	$L_{1-1000\mu m}$ $(10^{44}~{\rm erg\,s^{-1}})$
Abell 426	2.4 ± 0.7	7020 ± 66	6310 ± 440	0.40	9.2 ± 2.8
Abell 496	0.74 ± 0.30	60 ± 38	2210 ± 130	-3.02	2.7 ± 0.8
Virgo	$4.3 \pm 0.7 \times 10^{-2}$	520 ± 44	80 ± 99	1.25	$1.4 \pm 0.5 \times 10^{-2}$
Centaurus	0.20 ± 0.02	420 ± 37	890 ± 182	0.68	0.25 ± 0.08
Coma	—	< 141	< 408	—	< 0.47
Abell 1795	1.9 ± 0.5	< 144	< 354	—	< 3.3
Abell 2199	$0.99^{+0.15}_{-0.40}$	150 ± 26	510 ± 82	-0.13	0.95 ± 0.31
Abell 2597	$5.1^{+0.4}_{-1.5}$	80 ± 26	130 ± 134	0.63	2.7 ± 1.5

Table 13. The ages of the cooling flows, in units of Gyr, determined with the three methods described in Section 8. Column 2 lists the measurements of Allen & Fabian (1997) from their X-ray colour deprojection study (method 1). Columns 3 and 4 lists the results obtained from the comparisons of the mass deposition rates determined from the spectral and image deprojection analyses, both excluding (no $\Delta N_{\rm H}$) and including ($\Delta N_{\rm H}$) corrections for the effects of intrinsic absorption by a uniform screen of cold gas on the deprojection results (method 2). Column 5 summarizes the ages inferred from the breaks in the deprojected mass deposition profiles (method 3).

Cluster	METHOD 1	METHOD 2 (no $\Delta N_{\rm H}$)	($\Delta N_{\rm H}$)	METHOD 3
Abell 426	—	$2.16^{+0.40}_{-0.17}$	$1.69^{+0.23}_{-0.24}$	$3.10^{+0.54}_{-0.72}$
Abell 496	$3.3 - 6.8$	$9.44^{+14.0}_{-5.08}$	$2.94^{+1.53}_{-0.87}$	$4.85^{+0.69}_{-0.80}$
Virgo	—	$2.83^{+0.18}_{-0.29}$	$1.02^{+0.20}_{-0.16}$	$3.32^{+0.71}_{-0.63}$
Centaurus	—	$9.95^{+0.88}_{-0.97}$	$4.31^{+1.52}_{-0.74}$	—
Abell 1795	$3.6 - 6.7$	$5.41^{+0.95}_{-1.66}$	$2.87^{+0.36}_{-0.35}$	$6.76^{+1.29}_{-2.52}$
Abell 2199	$5.3 - 7.7$	$8.98^{+2.34}_{-3.19}$	$3.91^{+0.50}_{-0.72}$	$4.82^{+1.00}_{-0.84}$
Abell 2597	$2.5 - 5.1$	> 5.2	$2.51^{+0.59}_{-0.80}$	$3.30^{+2.28}_{-1.43}$

Table 14. The results from fits to the mass deposition profiles determined from the deprojection analysis with the broken power-law models. Only those data from radii interior to the 90 percentile upper limit to the cooling radii were included in the modelling, with the exception of the Virgo cluster where (due to uncertainties associated with the effects of the PSPC rib support structure) the analysis was limited to the central 78 kpc (15 arcmin) radius. Columns 2 and 3 list the slopes, η_1 and η_2, of the mass deposition profiles interior to and external to the break radii ($r_{\rm break}$; Column 4), respectively. Column 5 lists the mean cooling time of the cluster gas at the break radius (the errors on the cooling time are the differences relative to the values measured at the upper and lower limits to the break radii). Columns 6 and 7 list the integrated mass deposition rates within the break radii, with ($\dot{M}_{\rm C}(r < r_{\rm break})$) and without ($\dot{M}_{\rm I}(r < r_{\rm break})$) corrections for intrinsic absorption due to a uniform screen of cold gas. Error bars are pseudo-90 per cent confidence limits determined from the unweighted least-squares fits, assuming a reduced χ^2 value $\chi^2_\nu = 1.0$.

| Cluster	η_1 $(r < r_{\rm break})$	η_2 $(r > r_{\rm break})$	$r_{\rm break}$ (kpc)	$t_{\rm cool}(r_{\rm break})$ $(10^9 \ {\rm yr})$	$\dot{M}_{\rm I}(r < r_{\rm break})$ $(\,{\rm M}_\odot \ {\rm yr}^{-1}\,)$	$\dot{M}_{\rm C}(r < r_{\rm break})$ $(\,{\rm M}_\odot \ {\rm yr}^{-1}\,)$
Abell 426	$1.58^{+0.47}_{-0.26}$	$0.36^{+0.08}_{-0.08}$	82^{+9}_{-12}	$3.10^{+0.54}_{-0.72}$	417^{+29}_{-66}	785^{+110}_{-173}
Abell 496	$1.19^{+0.27}_{-0.17}$	$0.55^{+0.08}_{-0.08}$	77^{+11}_{-13}	$4.85^{+0.69}_{-0.80}$	87^{+10}_{-16}	188^{+56}_{-54}
Virgo	$0.94^{+0.09}_{-0.07}$	$0.65^{+0.06}_{-0.07}$	38^{+6}_{-5}	$3.32^{+0.71}_{-0.63}$	$12.8^{+1.1}_{-1.9}$	$29.6^{+3.8}_{-6.6}$
Abell 1795	$1.35^{+0.18}_{-0.16}$	$0.67^{+0.12}_{-0.11}$	119^{+19}_{-37}	$6.76^{+1.29}_{-2.52}$	305^{+60}_{-95}	632^{+215}_{-243}
Abell 2199	$1.69^{+0.25}_{-0.22}$	$0.92^{+0.06}_{-0.05}$	74^{+12}_{-8}	$4.82^{+1.00}_{-0.84}$	86^{+15}_{-12}	227^{+61}_{-57}
Abell 2597	$1.45^{+1.63}_{-0.73}$	$0.37^{+0.31}_{-0.37}$	91^{+72}_{-45}	$3.30^{+2.28}_{-1.43}$	309^{+160}_{-165}	895^{+562}_{-547}
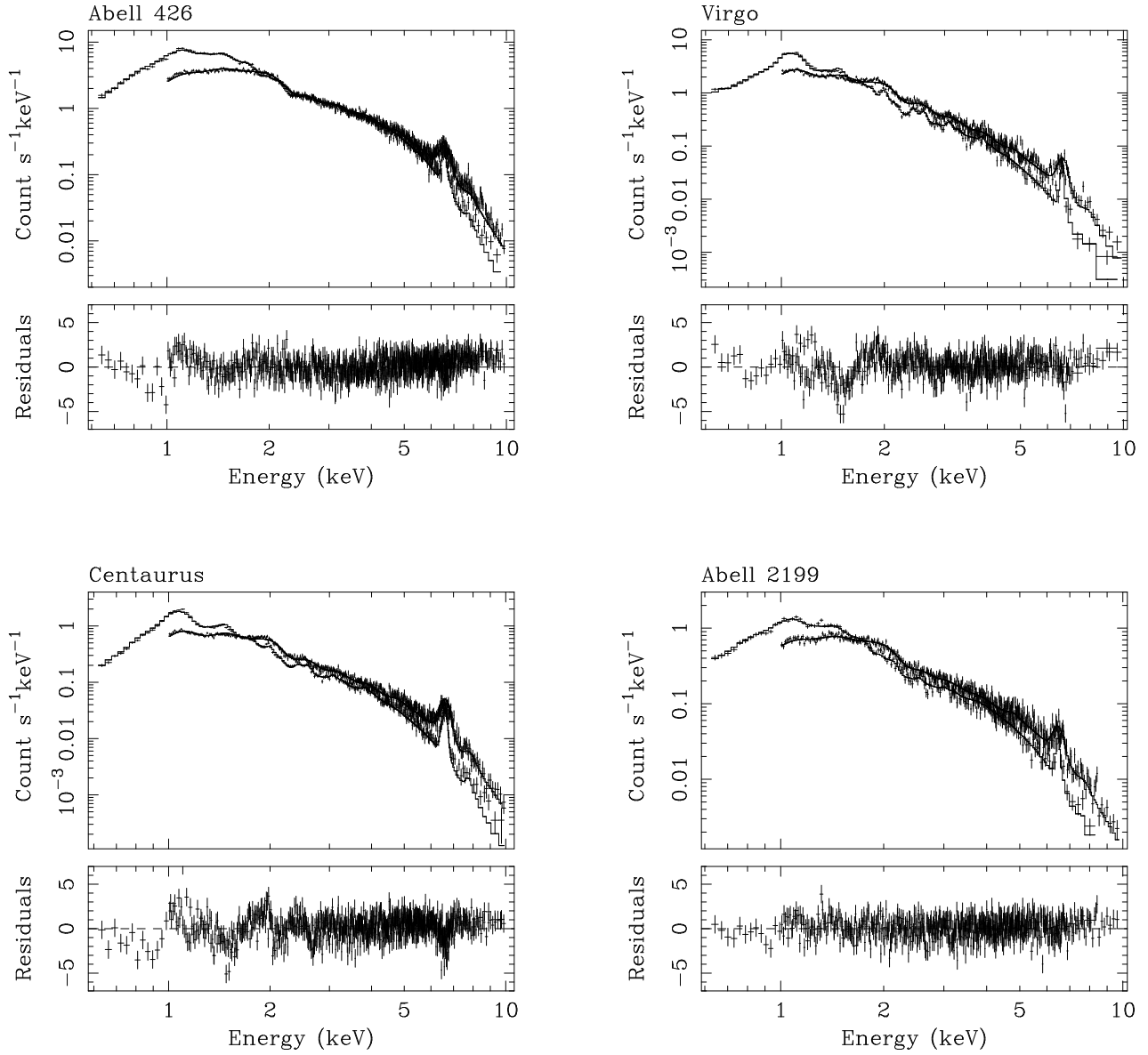
Figure 1. (Upper panels) The ASCA data and best-fitting models and (lower panels) residuals to the fits (in units of χ) for (clockwise from top left) Abell 426, the Virgo Cluster, Abell 2199 and the Centaurus Cluster. For clarity, only the S1 and G2 data and the results determined with spectral model C are shown.
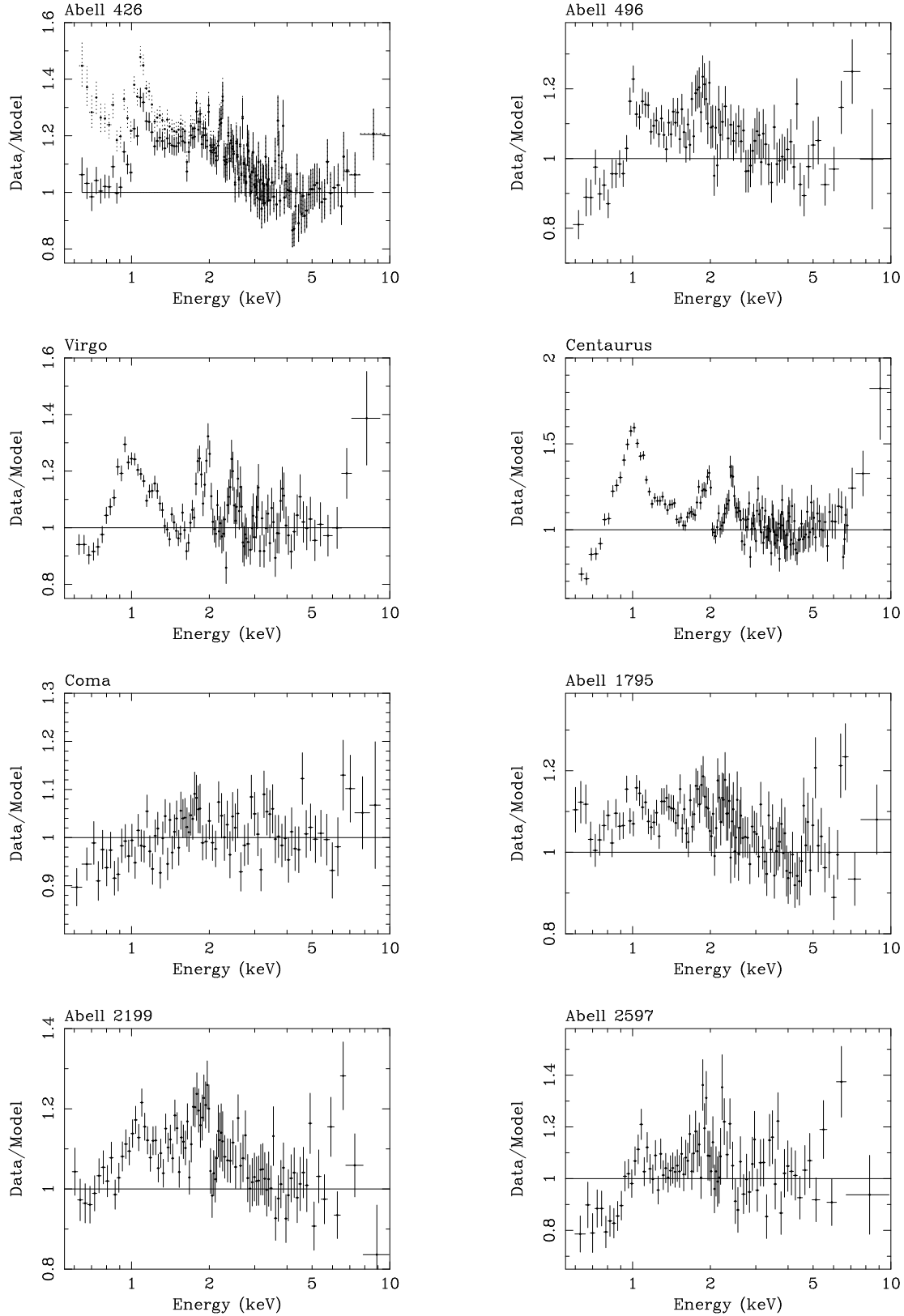
Figure 2. The residuals from fits to the SIS spectra in the $3.0 - 10.0$ keV energy range using a single-temperature emission model with Galactic absorption (model A). The best-fitting models have then been extrapolated to cover the full $0.6 - 10.0$ keV band of the SIS instruments. For the cooling-flow clusters, note the clear excess in the residuals at energies between ~ 0.8 and 3.0 keV (the region dominated dominated by the Fe-L, Mg, Si and S line complexes) indicating the presence of gas cooler than the ambient cluster temperatures. The deficits in the residuals at energies below 0.8 keV provide evidence for excess absorption. For Abell 426, the solid points show the results for an assumed Galactic column density of 1.0×10^{21} atom cm^{-2} (Section 3.3). The dotted points show the results using the nominal Dickey & Lockman (1990) value of 1.49×10^{21} atom cm^{-2}. Note also the positive residuals at high energies in the data for Abell 426, the Virgo Clusters and the Centaurus Cluster (see Section 4).
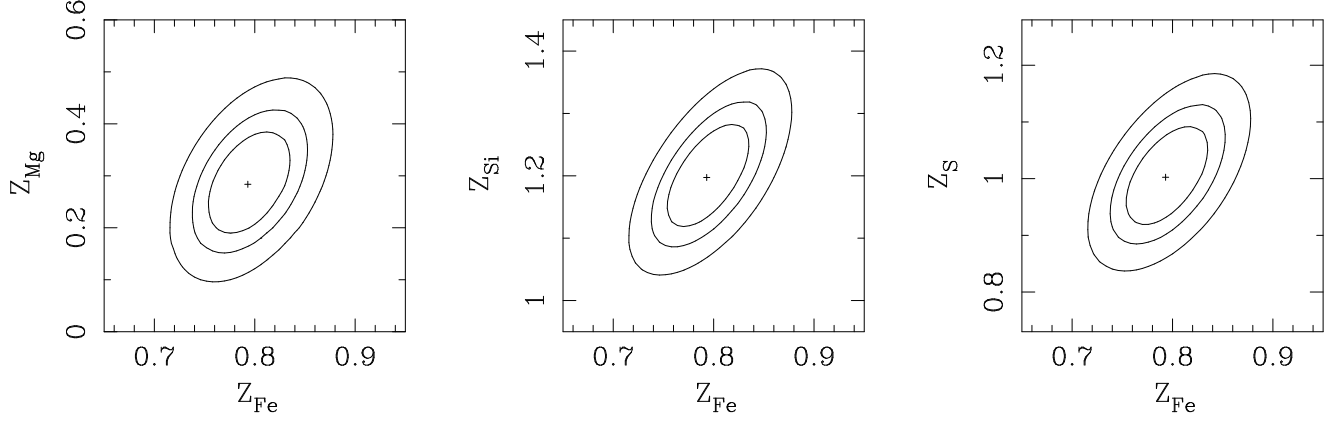
Figure 3. Joint confidence contours on the abundances of (left) Mg and Fe, (centre) Si and Fe, and (right) S and Fe determined from the ASCA SIS spectra for the Virgo Cluster. The solar photospheric abundance scale of Anders & Grevesse (1989) is assumed. Contours mark the regions of 68, 90 and 99 per cent confidence ($\Delta\chi^2 = 2.30, 4.61$ and 9.21, respectively).
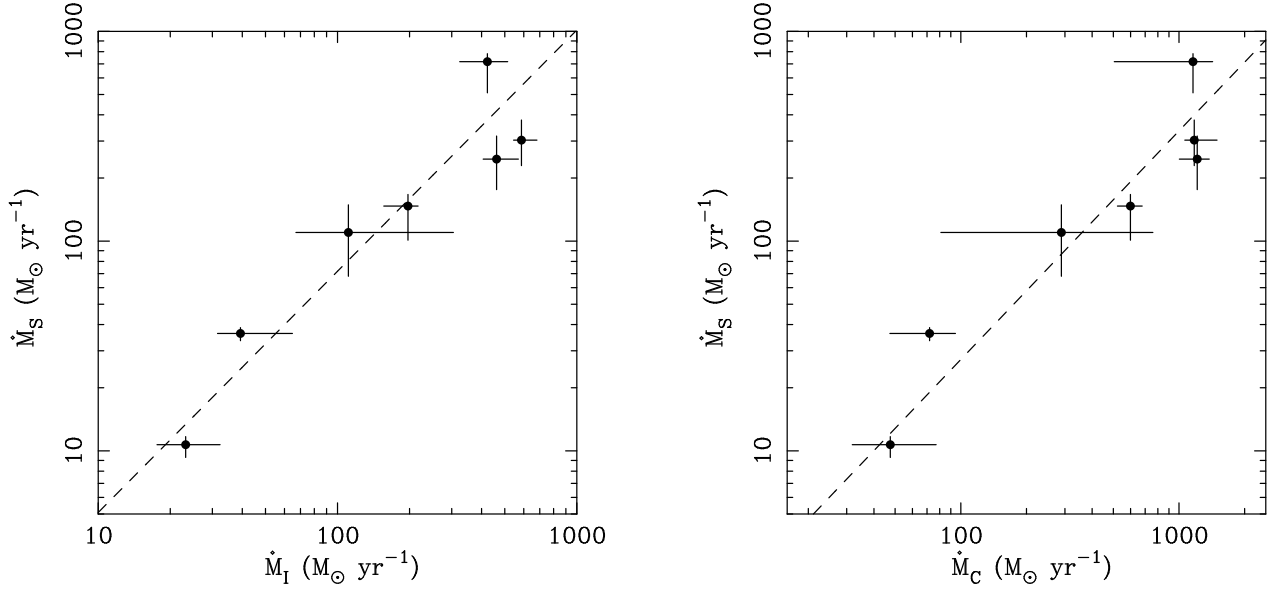

Figure 4. (a) The mass deposition rates determined from the ASCA spectra ($\dot{M}_S$) versus the values measured from the deprojection analysis of the ROSAT images ($\dot{M}_I$). No correction for the effects of intrinsic absorption on the deprojection results has been made. The dashed line is the best-fitting power-law model which has a slope, $Q = 1.15 \pm 0.33$ and a normalization, $P = 0.36 \pm 0.65$. (b) as for (a) but with the deprojection results corrected for the effects of intrinsic absorption by a uniform screen of cold gas with the best-fit parameters determined from the spectral analysis ($\dot{M}_C$). The best-fitting power-law model has a slope, $Q = 1.09 \pm 0.32$ and a normalization, $P = 0.18 \pm 0.37$. (Errors on P and Q are 1σ uncertainties determined by bootstrap re-sampling).
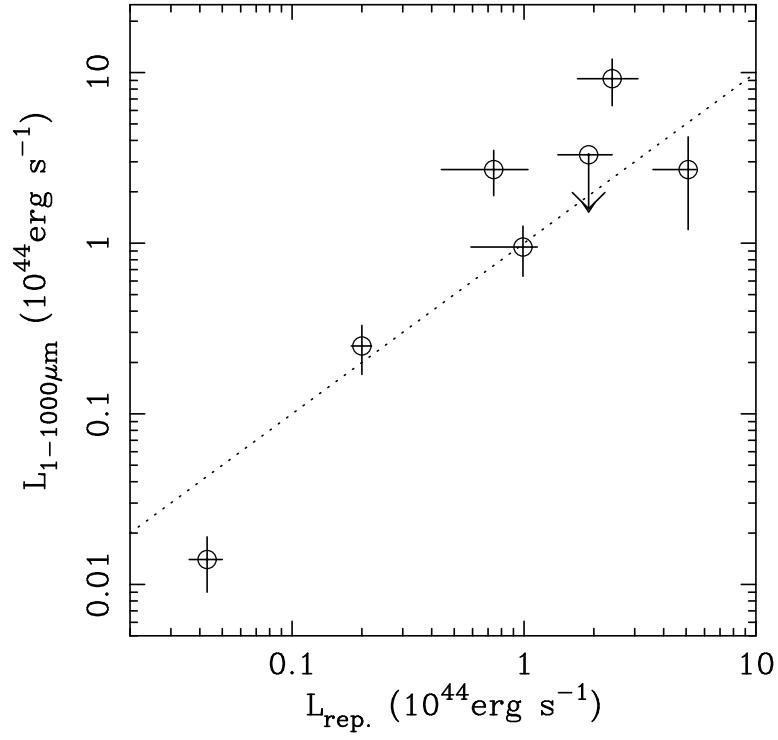
Figure 5. The $1 - 1000\mu$m luminosities determined from the IRAS 60 and 100μm fluxes (using equation 2) plotted as a function of the predicted reprocessed X-ray luminosities from the cooling flows. The dotted curve is the line of equality between the values.
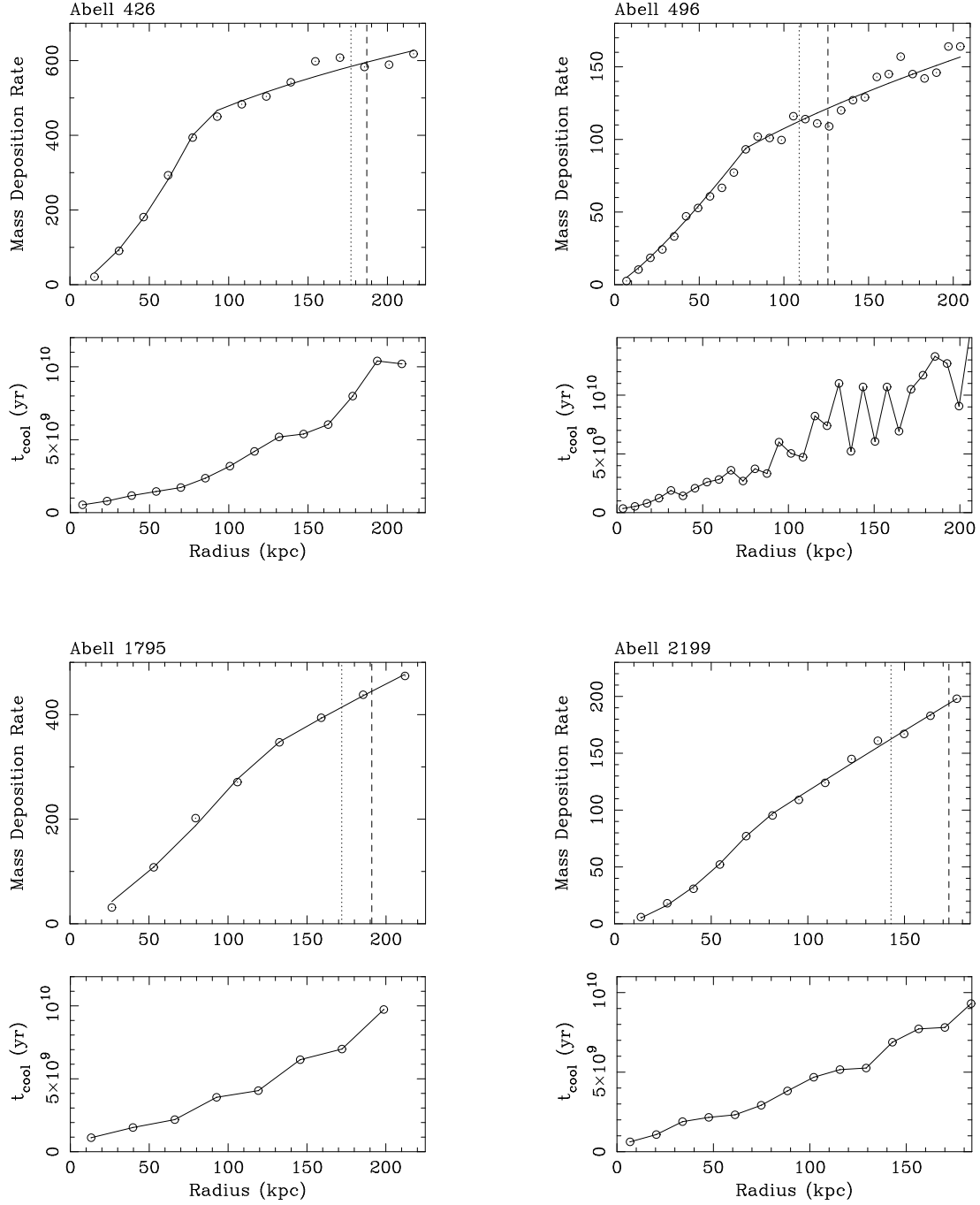
Figure 6. (Upper panels) The results from the fits with simple broken power-law models to the mass deposition profiles determined from the deprojection study (no correction for intrinsic absorption has been made). Only those data (marked with circles) from radii interior to the 90 percentile upper limit to the cooling radius were included in the fits. The vertical dashed lines mark the cooling radii in the clusters. The dotted lines mark the 90 percentile lower limits on the cooling radii. The lower panels show the mean cooling time of the cluster gas as a function of radius.
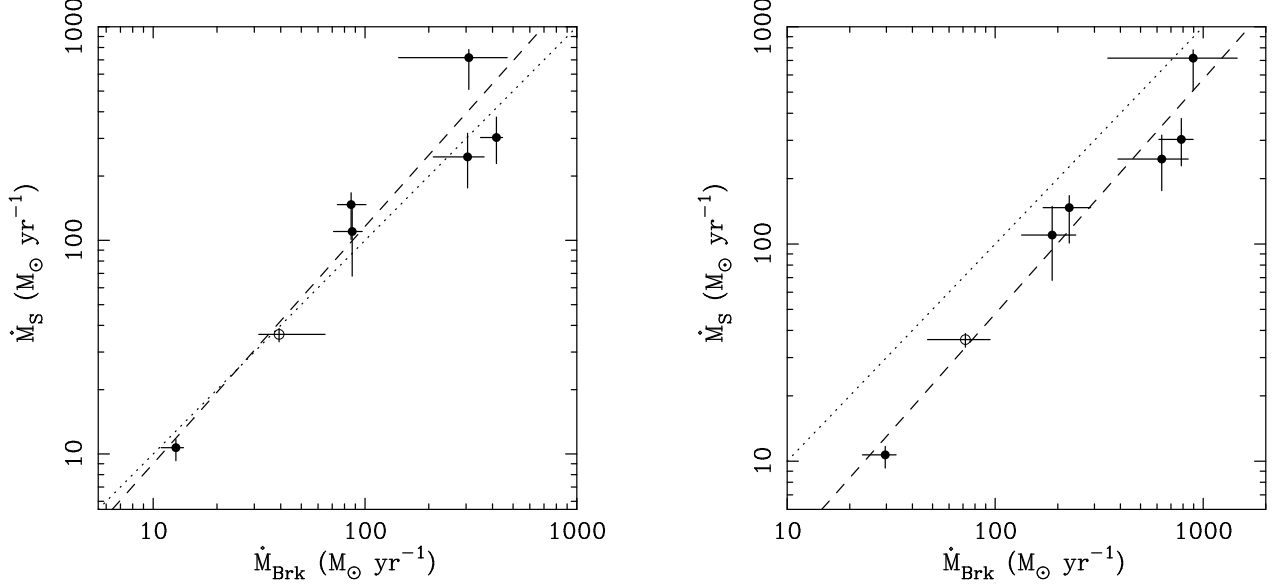
Figure 7. The mass deposition rates determined from the ASCA spectra ($\dot{M}_{\mathrm{S}}$) versus the values inferred from the breaks in the mass deposition profiles ($\dot{M}_{\mathrm{Brk}}$) determined from the deprojection study. The left and right panels show the results obtained without and with corrections for intrinsic absorption due to a uniform screen of cold gas, respectively. The dashed curves show the best fitting power-law models (see text for details). The dotted lines are the lines of equality ($y = x$) between the values. The Centaurus Cluster (plotted as an open circle) does not exhibit an obvious break in its mass deposition profile within the cooling radius and so we assume $\dot{M}_{\mathrm{Brk}} = \dot{M}_{\mathrm{C}}$ or $\dot{M}_{\mathrm{Brk}} = \dot{M}_{\mathrm{I}}$ from Table 10, as appropriate.
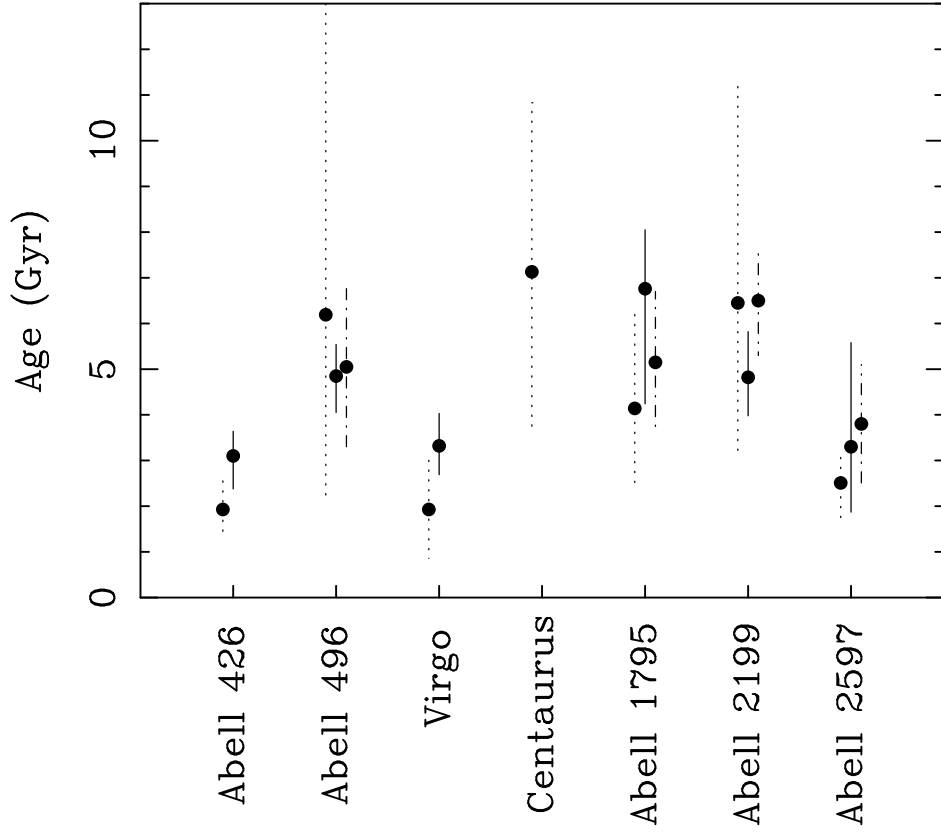
Figure 8. A comparison of the results on the ages of the cooling flows from the three methods described in Section 8. The dot-dashed lines are the results from the X-ray colour deprojection study of Allen & Fabian (1997; method 1). The dotted lines show the ages inferred from the comparison of the mass deposition rates determined from the spectral and image deprojection methods (method 2). For method 2, the average of the absorption-corrected and uncorrected results is shown, except for Abell 2597, for which the uncorrected result was unbounded and therefore, only the absorption-corrected result used. (The extent of the dotted curves mark the extrema obtained from the absorption-corrected and uncorrected analyses). The solid lines are the measurements based on the identifications of breaks in the mass deposition profiles (method 3).
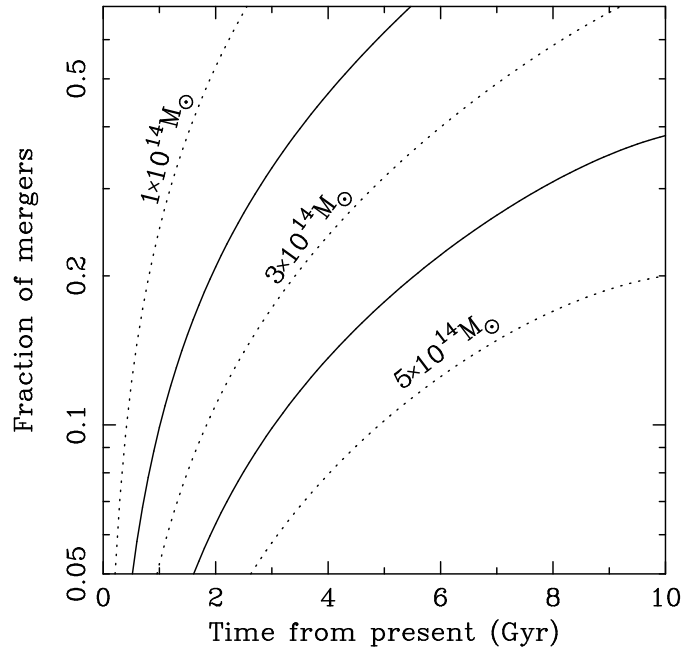
Figure 9. The fraction of current 10^{15} M$_\odot$ clusters which have experienced a merger with a subcluster of mass $1-5 \times 10^{14}$ M$_\odot$ (top to bottom) within a given time from the present ($\Omega = 1.0, \Lambda = 0, b = 1$ and a cosmic fluctuation index, $n = -1.5$ are assumed.)